Université de Montréal

Photon Elastic Scattering Background Events in the SuperCDMS SNOLAB Experiment

par

Noah Hassan

Département de physique
Faculté des arts et des sciences

Mémoire présenté en vue de l'obtention du grade de
Maître ès sciences (M.Sc.)
en Physique

November 12, 2023

Université de Montréal

Faculté des arts et des sciences

Ce mémoire intitulé

Photon Elastic Scattering Background Events in the SuperCDMS SNOLAB Experiment

présenté par

Noah Hassan

a été évalué par un jury composé des personnes suivantes :

Richard Mackenzie
(président-rapporteur)

Alan Robinson
(directeur de recherche)

Louis-André Hamel
(membre du jury)

Résumé

Alors que la nouvelle génération de détecteurs directs de matière sombre est en cours de construction, dans l'espoir de trouver de la matière sombre avec une masse inférieure au GeV, il est important de comprendre comment le rayonnement naturel peut produire un fond d'interactions à faible énergie. Cette thèse s'intéressera à la simulation de la diffusion élastique des rayons γ, une source possible de fonds pour les détecteurs de matière sombre sub-GeV. La simulation utilise le logiciel SuperSim basé sur Geant4 afin de modéliser l'expérience SuperCDMS SNOLAB. Une version modifiée du *G4JAEAElasticScatteringModel* appelée *CDMSJAEAElasticScatteringModel* a été mise en oeuvre dans SuperSim afin de simuler les mécanismes de diffusion de photon élastiques Rayleigh, nucléaire Thomson et Delbrück. Le *CDMSJAEAElasticScatteringModel* ajoute la possibilité pour les particules γ de déposer de l'énergie après avoir été diffusées élastiquement. La validité de ces deux modèles a été vérifiée et des erreurs dans le logicielle ont été rencontrées dans leur traitement des distributions d'angle de diffusion des photons qui déterminent les spectres d'énergie déposée. Les sections efficaces totales sont en accord avec la documentation et d'autres sources. Malgré les erreurs logicielles, la simulation définit une limite inférieure sur le taux de diffusion élastique des rayons γ de $\sim$ 0,01 et $\sim$ 0,035 photon diffusé élastiquement kg $^{-1}$ an^{-1} pour les détecteurs SuperCDMS SNOLAB au germanium et au silicium, respectivement. Ces limites inférieures sont définies à l'aide d'une coupure d'énergie de recul de 1 eV. Cela fait de la diffusion élastique des rayons γ une source importante de bruit de fond pour détecteurs SuperCDMS proposés avec des capacités de discrimination ER/NR à des énergies de recul à l'échelle eV.

Mots-clés: Matière sombre, Événements de fond à faible énergie, Diffusion élastique de photon, Physique des particules, SuperCDMS SNOLAB, Simulation Geant4.

Abstract

While the new generation of direct dark matter detectors are being built in the hopes of finding sub-GeV dark matter, it is important to understand how natural radiation can produce a background of low-energy interactions. This thesis will analyze simulating γ-ray elastic scattering, a possible source of background for sub-GeV dark matter detectors. The simulation uses Geant4-based SuperSim software in order to model the SuperCDMS SNOLAB experiment. A modified version of the *G4JAEAElasticScatteringModel* called *CDMSJAEAElasticScatteringModel* was implemented into SuperSim in order to simulate the Rayleigh, nuclear Thomson and Delbrück γ-ray elastic scattering mechanisms. The *CDMSJAEAElasticScatteringModel* adds the ability for the γ particles to deposit energy after being elastically scattered. The validity of both these models was checked, and errors were encountered in their treatment of photon scattering angle distributions which determine the deposited energy spectra. The total cross sections are consistent with the documentation and other sources. Despite the bug, the simulation does set a lower bound on the γ-ray elastic scattering rate of ~ 0.01 and ~ 0.035 elastically scattered photon kg^{-1} $year^{-1}$ for germanium and silicon SuperCDMS SNOLAB detectors, respectively. These lower bounds are set using a 1 eV recoil energy cutoff. In conclusion, γ-ray elastic scattering a significant source of background for proposed SuperCDMS detectors with ER/NR discrimination capabilities at eV-scale recoil energies.

Keywords: Dark matter, Low energy background events, Photon elastic scattering, Particle physics, SuperCDMS SNOLAB, Geant4 simulation.

Contents

Résumé 5

Abstract 7

List of tables 11

List of figures 13

List of acronyms and abbreviations 17

Acknowledgments 19

Chapter 1. Dark matter direct detection 21

1.1. A general approach to direct detection event rates 22

1.2. Dark matter density and velocity distribution 23

1.3. Neutrino background 26

Chapter 2. SuperCDMS SNOLAB sensitivity 31

2.1. The detectors 32

2.2. Cryostat and shielding 35

2.3. Sources of Background 36

2.3.1. Impurities in the detector crystals 37

2.3.2. Material internal activation 37

2.3.3. Material internal contamination 39

2.3.4. Non-line-of-sight surfaces 39

2.3.5. Line-of-sight surfaces 40

2.3.6. SNOLABs cavern environment 41

2.3.7. Neutron backgrounds 42

2.3.8. Cosmic rays 42

2.3.9. Coherent neutrino interactions 42

2.4. Cuts and cross section upper limits 43

Chapter 3. Simulating γ-ray elastic and coherent scattering 47

3.1. Motivation and preliminary estimate 47

3.2. SuperSim and Geant4 49

3.3. γ-ray elastic and coherent scattering 50

3.3.1. Coherent scattering differential cross section 51

3.3.2. Scattering amplitudes 51

3.4. G4JAEAElasticScatteringModel 54

3.4.1. Data files 54

3.4.2. Important functions 56

3.4.3. Problems with the model 57

3.5. CDMSJAEAElasticScatteringModel and future improvements 58

Chapter 4. The simulation 61

Chapter 5. Conclusion 65

Références bibliographiques 67

List of tables

2.1 The contamination rates in μBq/kg for the radioisotopes coming from activated materials in the SuperCDMS experiment. The assumptions used are the production rates mentioned in the text, a sea-level exposure of 90 days followed by a 90 day underground "cooling" period for copper in the housings and towers and a sea-level exposure of 180 days followed by a 180 day "cooling" period for the copper cryostat cans. The contamination rates and assumptions used come from Reference [**3**] where the assumptions for the other elements are not mentioned. In the creation of Figure 2.2, only the isotopes ^{57}Co, ^{58}Co, ^{60}Co and ^{54}Mn are taken into account for the housings and towers with ^{60}Co being the only one taken into account for the cryostat. 38

2.2 The assumed radioisotope impurity concentrations coming from contaminants of SuperCDMS SNOLAB materials. The impurity concentrations for copper and Lead are taken from Reference [**6**], cirlex, μ-metal, and high-density polyethylene (HDPE) are taken from Reference [**38**] and Kevlar is taken from Reference [**7**]. The impurity concentrations for polypropylene and water are assumed to be the same as HDPE as a conservative estimation. 39

3.1 Comparison of uranium differential cross section (b/st) as a function of scattering angle (deg) for an incident photon energy of 40 keV. The second column shows the values mentioned in the model's documentation [**43**], and the third column shows the values obtained in the manner implemented by the *G4JAEAElasticScatteringModel* code. The fourth column is the quotient of the third and second columns. 58

List of figures

1.1 A plot of the differential rate as a function of recoil energy for $m_\chi = 10$ GeV/c^2 and $\sigma_{\chi N} = 10^{-42}$ cm^2. The figure has six separate curves for different atomic numbers A and nuclear mass m_T representing germanium, silicon, xenon, argon, tungsten, and bismuth. 26

1.2 The differential coherent neutrino scattering rate as a function of recoil energy for a germanium target. As mentioned in the text, 16 different neutrino spectra are present (data 1-16) with data 17 being the sum total. 29

1.3 The differential coherent neutrino scattering rate as a function of recoil energy for a silicon target. As mentioned in the text, 16 different neutrino spectra are present (data 1-16) with data 17 being the sum total. 29

2.1 Cross section (cm^2) as a function of WIMP mass (GeV/c^2) of past spin-independent elastic WIMP-nucleus scattering experiments using the standard parameters for an isothermal WIMP halo: $\rho_0 = 0.3$ GeV/c^2/cm^3, $v_\chi = 220$ km/s, $v_{esc} = 544$ km/s. Figure taken from Reference [**13**]. 31

2.2 Projected exclusion sensitivity for the SuperCDMS SNOLAB direct detection dark matter experiment. The vertical axis is the spin-independent WIMP-nucleon cross section under standard halo assumptions while the horizontal axis is the WIMP mass. Figure taken from Reference [**3**]. 32

2.3 Arrangement of the different channels for the HV and iZIP detectors where each color represents a different phonon channel. The wedge-shaped channels on the bottom surface of the HV and iZIP detectors are rotated by 60°and 45°respectively with respect to the top surface. One of the iZIP's ionization channels is interleaved with the phonon channel represented by the dark blue outer ring while the other ionization channel is interleaved with all the other phonon channels. This figure is taken from Ref [**3**]. 33

2.4 The experimental setup of the shielding, cryogenic system, and seismic platform for the SuperCDMS SNOLAB experiment. Figure taken from [**3**]. 35

2.5 A detailed layout of the tower mechanical support and instrumentation for one of six detectors in a tower used in the SuperCDMS SNOLAB experiment. Figure taken from [**3**]. 41

2.6 Background spectra before (left) and after (right) analysis cuts in Si (top) and Ge (bottom) HV detectors as a function of nuclear recoil energy (keVnr). ERs from Compton γ-rays, ^{3}H, and ^{32}Si are grouped together and represented by the red line. The Ge activation lines are in grey. The surface betas are represented by the green line, surface ^{206}Pb by the orange line, neutrons by the blue line, and neutrinos by the cyan line. The black line represents the total signal. Figure taken from Reference [**3**]. 44

2.7 Background spectra before (left) and after (right) analysis cuts in Si (top) and Ge (bottom) iZIP detectors as a function of nuclear recoil energy (keVnr). ERs from Compton γ-rays, ^{3}H and ^{32}Si are grouped together and represented by the red line. The Ge activation lines are in grey. The surface betas are represented by the green line, surface ^{206}Pb by the orange line, neutrons by the blue line and neutrinos by the the cyan line. The black line represents the total signal. Figure taken from Reference [**3**]. 45

3.1 Differential rate as a function of nuclear recoil energy for a germanium (black) or silicon (red) target inside an infinite copper sphere with a contamination rate of 0.04 mBq/kg. 49

3.2 The absorption first, two vertex Feynman diagram contribution to the $S^{(2)}$. From left to right, the first vertex represents the moment when $t = t_1$ while the second vertex represents the moment when $t = t_2$. 53

3.3 The emission first, two vertex Feynman diagram contribution to $S^{(2)}$. From left to right, the first vertex represents the moment when $t = t_1$ while the second vertex represents the moment when $t = t_2$. 53

3.4 Rayleigh scattering amplitudes from the RTAB data points superimposed with the interpolation points for a target material of atomic number 50 and three incident photon energies. The RTAB data is represented by the red points while the interpolation is represented by the blue lines. Figure taken from Reference [**43**] 55

3.5 Delbrück scattering amplitudes for the original data points taken from Reference [**23**] superimposed with the interpolation points for a target material of atomic

number 50 and three incident photon energies. The original data is represented by the red points while the interpolation is represented by the blue lines. Figure taken from Reference [**43**] 56

4.1 Photon elastic scattering differential rate (events keV^{-1} kg^{-1} year^{-1}) as a function of recoil energy (keV). Data from simulating the entire SuperCDMS SNOLAB geometry using ^{60}Co and ^{232}Th inside the housing as a source. The photon elastic scattering differential rate for all SuperCDMS SNOLAB background sources is expected to be over one order of magnitude greater than shown. The histogram has 300 bins evenly distributed over the range of 0 to 0.03 keV. 62

4.2 Photon elastic scattering (bins) and total CNS (line) differential rate (events keV^{-1} kg^{-1} year^{-1}) as a function of recoil energy (keV) for germanium. Data from simulating the entire SuperCDMS SNOLAB geometry using ^{60}Co and ^{232}Th inside the housing as a source. The photon elastic scattering differential rate for all SuperCDMS SNOLAB background sources is expected to be over one order of magnitude greater than shown. The histogram has 300 bins evenly distributed over the range 0 to 0.03 keV. The CNS differential rate accounts for all CNS sources mentioned in Section 1.3. 63

4.3 Photon elastic scattering (bins) and total CNS (line) differential rate (events keV^{-1} kg^{-1} year^{-1}) as a function of recoil energy (keV) for silicon. Data from simulating the entire SuperCDMS SNOLAB geometry using ^{60}Co and ^{232}Th inside the housing as a source. The photon elastic scattering differential rate for all SuperCDMS SNOLAB background sources is expected to be over one order of magnitude greater than shown. The histogram has 300 bins evenly distributed over the range 0 to 0.03 keV. The CNS differential rate accounts for all CNS sources mentioned in Section 1.3. 64

List of acronyms and abbreviations

ER	*Electron recoil*
NR	*Nuclear recoil*
CNS	*Coherent neutrino scattering*
NTL	*Neganov-Trofimov-Luke*
QET	*Quasiparticle trap-assisted Electrothermal-feedback Transition-edge sensor*
HDPE	*High-density polyethylene*
JAEA	*Japan Atomic Energy Agency*
RTAB	*Rayleigh scattering database*

Acknowledgments

I would like to begin by thanking the Department of Physics at Université de Montreal for allowing me the opportunity to take part in the Master's program and thesis project. I am grateful for my experience and ability to grow as a learner. I would like to thank my research supervisor, Dr. Alan Robinson, for his consistent presence and support throughout my Master's. I am very grateful for all the time he has spent helping me gain a greater understanding of physics. His optimistic outlook was well appreciated and helped instill confidence in my abilities. I would also like to thank Dr. Birgit Zatschler for helping advance my learning of Geant4 and SuperSim. The questions she has answered and the resources that she has provided me with have been fundamental to the completion of this thesis. Finally, I would like to show my gratitude to my friends and family for their unwavering love and support.

Chapter 1

Dark matter direct detection

There are many methods that can be used for dark matter detection. These methods can generally be separated into three distinct categories: searches at particle accelerators/detectors, astrophysical detection, and direct detection. For particle accelerator and collider detection, dark matter particles presumably do not interact with the detectors, meaning dark matter can only be detected by reconstructing missing energy and momentum from measured particles [**53**]. When it comes to astrophysical detection, experimenters look for macroscopic effects dark matter might have on astrophysical systems. These effects include gravitational lensing and the debris from dark matter particles that decay or annihilate one another creating neutrinos, gammas, or antimatter particles [**26**]. Direct detection experiments generally hope to measure elastic or inelastic scattering of dark matter with the nuclei or electrons of the detector material. These scattering events are known as nuclear recoils (NRs) or electron recoils (ERs) depending on what scattered the dark matter.

This chapter aims to derive key signals in direct detection experiments, notably, the expected spin-independent dark matter event rate and the coherent neutrino scattering rate. Both of these signals are important when setting priorities on which background sources to best understand. The dark matter rate sets a baseline for the expected dark matter signal. As will be mentioned in Chapter 2, SuperCDMS SNOLAB backgrounds are normally suppressed through ER/NR discrimination. While for many models dark matter couples well to nuclei, only relatively rare natural radiation interactions produce nuclear recoils: notably neutron scattering and coherent neutrino scattering. The same can be said about the photon elastic scattering background signal. Therefore the comparison of these two rates with the expected photon elastic scattering rates discussed in Section 3.1 and Chapter 4 can motivate the development of techniques to discriminate against photon elastic scattering backgrounds. This chapter is based on the book "An Introduction to Particle Dark Matter" by Stefano Profumo [**46**] and the paper "Review of mathematics, numerical factors, and corrections for dark matter experiments based on elastic nuclear recoil" by Lewin and Smith [**37**].

1.1. A general approach to direct detection event rates

In direct detection experiments, it is important to define a detector event rate R which represents the number of scattering events per unit time, energy, and detector mass for an event with nuclear recoil energy E_R. A general differential rate dR/dE_R can be written as the number of target nuclei N_T multiplied by the average dark matter flux Θ and the differential cross section $d\sigma/dE_R$.

$$\frac{dR}{dE_R} = N_T \Theta \frac{d\sigma}{dE_R}. \tag{1.1.1}$$

The average dark matter flux can more generally be written as the average dark matter number density n_χ multiplied by the dark matter particle's velocity relative to the target v_χ (throughout this thesis, χ will be used to represent a generic dark matter particle)

$$\frac{dR}{dE_R} = N_T n_\chi \left\langle v_\chi \frac{d\sigma}{dE_R} \right\rangle \tag{1.1.2}$$

where $n_\chi = \rho_{DM}/m_\chi$ (the dark matter mass density over the mass of a dark matter particle). The $\langle v_\chi d\sigma/dE_R \rangle$ is the averaged-out velocity multiplied by the averaged-out differential cross section assuming the differential cross section depends on the dark matter's velocity [**46**].

In the center of mass frame where the net momentum is zero, we have the dark matter particle's initial (final) momentum $\vec{p}$ ($\vec{p}'$) equal to the target's initial (final) momentum $\vec{k}_T$ ($\vec{k}'_T$):

$$\vec{p} = -\vec{k}_T = \mu_T \vec{v}_\chi \tag{1.1.3}$$

$$\vec{p}' = -\vec{k}'_T = \vec{q} + \mu_T \vec{v}_\chi \tag{1.1.4}$$

where $\vec{q}$ is the momentum transfer ($\vec{q} = \vec{p}' - \vec{p}$) and μ_T is the dark matter-nucleus reduced mass ($\mu_T = m_\chi m_T/(m_\chi + m_T)$), where m_T is the mass of the target nucleus.

Knowing $|\vec{p}| = |\vec{p}'|$ for elastic scattering in the center of mass frame, if we subtract Equation 1.1.4 from Equation 1.1.3 and square both sides we have:

$$\begin{aligned} \frac{|\vec{q}|^2}{2} &= |\vec{p}|^2 - \vec{p} \cdot \vec{p}' \\ &= |\vec{p}|^2 (1 - \cos\theta) \\ &= \mu_T^2 v_\chi^2 (1 - \cos\theta) \end{aligned}$$

where θ is the scattering angle in the center of mass frame. Finally, dividing by the mass of the target m_T allows the calculation of the recoil energy E_R (energy transferred from a dark matter particle of mass m_χ to a target with nuclear mass m_T)

$$\begin{aligned} E_R &= \frac{|\vec{q}|^2}{2m_T} \\ &= \frac{\mu_T^2}{m_T} v_\chi^2 (1 - \cos\theta). \end{aligned} \tag{1.1.5}$$

The minimum velocity v_{min} a dark matter particle needs in order to deposit a recoil energy E_R into the target can be found by letting $\cos\theta = -1$ (back-scattering).

$$v_{min} = \sqrt{\frac{m_T E_R}{2\mu_T^2}} = \frac{q}{2\mu_T}. \tag{1.1.6}$$

For a given velocity v, the differential recoil energy is

$$dE_R = (d\,\cos\theta)(\frac{\mu_T^2}{m_T})v^2. \tag{1.1.7}$$

Substituting Equation 1.1.7 into Equation 1.1.2 gives

$$\frac{dR}{dE_R} = N_T n_\chi \left\langle \frac{m_T}{\mu_T^2 v} \frac{d\,\sigma}{d\,\cos\theta} \right\rangle. \tag{1.1.8}$$

By substituting $n_\chi = \rho_{DM}/m_\chi$, knowing μ_T and m_T are constants and by writing the velocity average explicitly, we get the general formula

$$\frac{dR}{dE_R} = N_T \frac{\rho_{DM} m_T}{m_\chi \mu_T^2} \int_{v_{min}}^{v_{max}} d^3v \frac{f(v)}{v} \frac{d\,\sigma}{d\,\cos\theta} \tag{1.1.9}$$

where $f(v)$ is a dark matter halo velocity probability distribution function of choice, and v_{min} and v_{max} are the minimum and maximum velocities a dark matter particle can have to cause a nuclear recoil E_R.

1.2. Dark matter density and velocity distribution

The goal of this section is to make simplifications in order to get a less general version of Equation 1.1.9 which would lead to an approximation of dR/dE_R for Earth based detectors made of a single material. Certain assumptions will be made on $f(v)$, σ, and v_{max} in order to plot the expected dR/dE_R. The information in this section is based on the Lewin and Smith paper [**37**] unless cited otherwise.

As seen in Section 1.1, the event rate derivative with respect to recoil energy depends on the dark matter halo velocity probability distribution function $f(v)$. Since the dark matter detector is located on Earth, in orbit with the Sun, with the solar system moving through the

Galaxy, it is useful to redefine $f(v)$ as $f(\vec{v},\vec{v}_E)$ where $\vec{v}$ is the velocity of the (Earth-borne) target and $\vec{v}_E$ is the Earth's velocity relative to the dark matter distribution. As well, let v_{max} be the galactic escape velocity v_{esc}. Let us assume a Maxwellian dark matter velocity distribution:

$$g(\vec{v},\vec{v}_E) = e^{-(\vec{v}+\vec{v}_E)^2/v_\chi^2} \tag{1.2.1}$$

therefore,

$$f(\vec{v},\vec{v}_E) = \frac{e^{-(\vec{v}+\vec{v}_E)^2/v_\chi^2}}{k} \tag{1.2.2}$$

where k is a normalization constant such that,

$$\int_{v_{min}}^{v_{esc}} \frac{e^{-(\vec{v}+\vec{v}_E)^2/v_\chi^2}}{k}\, d^3\vec{v} = 1 \tag{1.2.3}$$

therefore,

$$k = \int_0^{2\pi} d\phi \int_{-1}^{+1} d(\cos\theta) \int_{v_{min}}^{v_{esc}} e^{-(\vec{v}+\vec{v}_E)^2/v_\chi^2} v^2 dv. \tag{1.2.4}$$

If we define k_0 as k when $v_{esc} = \infty$ and $v_{min} = 0$,

$$k_0 = (\pi v_\chi^2)^{3/2}. \tag{1.2.5}$$

By defining k_1 as k when $v_{esc} = |\vec{v} + \vec{v}_E|$,

$$k_1 = k_0 \left[\mathrm{erf}(\frac{v_{esc}}{v_\chi}) - \frac{2}{\pi^{1/2}} \frac{v_{esc}}{v_\chi} e^{v_{esc}^2/v_\chi^2} \right]. \tag{1.2.6}$$

When the momentum transfer between the dark matter particle and the target ($q = \sqrt{2m_T E_R}$) is much smaller than Planck's constant over the nuclear radius then the cross section can be considered constant with respect to velocity [**22**]. Since the SuperCDMS SNOLAB experiment is interested in the sub 10 GeV/c^2 mass range for dark matter, this approximation should not have a significant effect on the event rate. Furthermore, with the assumption that the scattering is isotropic (uniform in $\cos\theta$) then $d\sigma/d\cos\theta = \sigma/2$ where σ is the total dark matter cross section. Using these approximations, Equation 1.1.9 can be written:

$$\frac{dR}{dE_R} = \frac{N_0}{A} \frac{\rho_{DM} m_T}{m_\chi \mu_T^2} \frac{\sigma}{2} \int_{v_{min}}^{v_{max}} d^3v \frac{f(v)}{v}$$

where N_T was replaced with Avogadro's number N_0 and the target atomic mass A in atomic mass units (amu). We can define R_0 as the event rate per unit mass for $v_E = 0$ and $v_{esc} = \infty$,

$$R_0 = \frac{2}{\pi^{1/2}} \frac{N_0}{A} \frac{\rho_{DM}}{m_\chi} \sigma v_\chi. \tag{1.2.7}$$

If we also define

$$r = \frac{4 m_\chi m_T}{(m_\chi + m_T)^2}$$

and the average dark matter kinetic energy

$$E_0 = \frac{1}{2} m_\chi v_\chi^2$$

we arrive at Equation 3.9 from the Lewin and Smith paper [**37**]

$$\frac{dR}{dE_R} = \frac{R_0}{E_0 r} \frac{k_0}{k} \frac{1}{2\pi v_0^2} \int_{v_{min}}^{v_{max}} \frac{1}{v} f(\vec{v},\vec{v}_E) d^3 v. \tag{1.2.8}$$

Solving Equation 1.2.8 for a non-zero v_E and finite v_{esc} gives:

$$\frac{dR(v_E, v_{esc})}{dE_R} = \frac{k_0}{k_1} \left[\frac{dR(v_E,\infty)}{dE_R} - \frac{R_0}{E_0 r} e^{-v_{esc}^2/v_\chi^2} \right] \tag{1.2.9}$$

where

$$\frac{dR(v_E,\infty)}{dE_R} = \frac{R_0}{E_0 r} \frac{\pi^{1/2}}{4} \frac{v_\chi}{v_E} \left[\mathrm{erf}\left(\frac{v_{min} + v_E}{v_\chi} \right) - \mathrm{erf}\left(\frac{v_{min} - v_E}{v_\chi} \right) \right]. \tag{1.2.10}$$

This allows the opportunity to think about the left-hand and right-hand sides of Equation 1.2.9. The left-hand side is what is experimentally measured and therefore, the role of experimenters is to lower and reject background events in order to detect these rare dark matter recoils. Sources of background for the SuperCDMS SNOLAB experiment are discussed in Section 2.3. The right-hand side depends on a few input parameters: v_χ, ρ_{DM}, v_{esc}, v_E, A, m_T, m_χ, and σ. The input parameters v_χ, ρ_{DM}, v_{esc}, v_E, can all be approximated from astrophysical observations while the target properties A and m_T are well documented. The cross section σ can be approximated using:

$$\sigma \simeq A^2 \left(\frac{\mu_T}{\mu_p} \right) \sigma_{\chi N} F_H(q^2) \tag{1.2.11}$$

where $\mu_p = m_\chi m_p/(m_\chi + m_p)$ is the reduced mass of the dark matter particle and the proton m_p, $\sigma_{\chi N}$ is the spin-independent cross section between dark matter and a target nucleus and $F_H(q^2)$ is the Helm form factor correction defined by Equation 1.3.3.

The standard rotational velocity for local objects with respect to our galaxy is 220 km/s [**33**]. This gives an estimate $v_\chi = 220$ km/s. Estimates for ρ_{DM} for a spherical halo are in the range of 0.2 GeVc^{-2}cm^{-3} $\leq \rho_{DM} \leq$ 0.4 GeVc^{-2}cm^{-3} leading to the adoption of

$\rho = 0.3$ GeVc^{-2}cm^{-3} as the central value [**37**]. The escape velocity v_{esc} is between 498 km/s $< v_{esc} <$ 608 km/s (90% confidence), with a median likelihood of 544 km/s [**51**]. For this reason, we take $v_{esc} = 544$ km/s. The Earth's velocity with respect to dark matter can be estimated to $v_E = 12$ km/s +220 km/s where the 12 km/s is the Sun's peculiar velocity relative to nearby [**49**]. Although the Earth is in motion with respect to the Sun, we can approximate Earth's average velocity to be the same as that of the Sun.

With all these parameters set, Equation 1.2.9 gives the differential recoil energy as a function of recoil energy, spin-independent cross section $\sigma_{\chi N}$, and dark matter particle mass. The SuperCDMS SNOLAB experiment is interested in detecting dark matter particles with $m_\chi \lesssim 10$ GeV/c^2, motivating Figure 1.1 which shows a plot of the differential rate as a function of recoil energy of germanium, silicon, xenon, argon, tungsten, and bismuth for a dark matter particle of mass 10 GeV/c^2 and $\sigma_{\chi N} = 10^{-42}$ cm^2. This figure will later be compared with the differential photon elastic scattering rates in Sections 3.1 and 4.

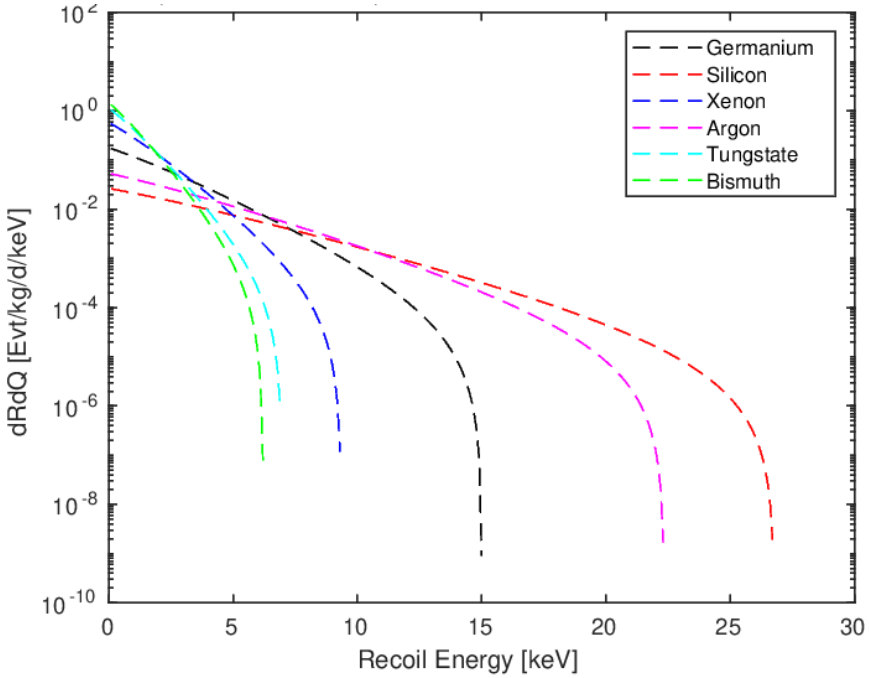

Fig. 1.1. A plot of the differential rate as a function of recoil energy for $m_\chi = 10$ GeV/c^2 and $\sigma_{\chi N} = 10^{-42}$ cm^2. The figure has six separate curves for different atomic numbers A and nuclear mass m_T representing germanium, silicon, xenon, argon, tungsten, and bismuth.

1.3. Neutrino background

Coherent neutrino scattering is one of the most important forms of background for modern dark matter direct detection experiments since its signal cannot currently be distinguished from a dark matter signal. This is the reason it is important to have a good estimate of the

expected coherent neutrino scattering event rate for any dark matter experiment. The goal of this section is to give an approximation for the expected differential rate as a function of recoil energy. This is similar to Section 1.2; however, it differs by not having to approximate a velocity distribution, but by defining different neutrino sources with a corresponding energy spectrum for each source. These energy spectra are taken from the SuperCDMS internal database.

By using Equation 1.1.1 to get the differential recoil energy, three values are needed: the number of target nuclei N_T, the neutrino flux Θ and the differential cross section $d\sigma/dE_R$. The differential cross section for coherent neutrino scattering can be expressed as:

$$\frac{d\sigma}{dE_R} = \frac{G_F^2}{4\pi} Q_W^2 m_T \left(1 - \frac{m_T E_R}{2E_v^2}\right) F(q^2)^2 \tag{1.3.1}$$

where G_F is the precisely known Fermi constant, $F(q^2)$ is a form factor correction that depends on the square of the momentum transfer q and

$$Q_W = N - (1 - 4\sin^2(\theta_W))Z \tag{1.3.2}$$

which represents the weak charge, where N is the number of neutrons and Z the number of protons of the target material with mass m_T [**5**].

A common choice for the form factor used to calculate the differential coherent neutrino scattering rate is the Helm form factor

$$F_H(q^2) = 3\frac{j_1(qr_n)}{qr_n} e^{-q^2 s^2/2} \tag{1.3.3}$$

where $j_1(x) = \sin(x)/x^2 - \cos(x)/x$ is the spherical Bessel function of order one, s is the nuclear skin thickness and r_n is the effective nuclear radius [**50**]. It is important to note that the Helm form factor is an approximation that is superseded by nucleus-specific models when higher accuracy is required.

The effective nuclear radius can be written:

$$r_n^2 = c^2 + \frac{7}{3}\pi^2 a^2 - 5s^2 \tag{1.3.4}$$

where a and c are parameters in the Fermi charge distribution which can be experimentally calculated. According to Fricke et al., $a \simeq 0.52$ fm [**25**]. Lewin and Smith recommend $s \simeq 0.9$ fm and c can be written as

$$c = (1.32A^{1/3} - 0.6) \text{ fm}. \tag{1.3.5}$$

Since the neutrino differential cross section is well defined, we must choose which neutrino sources to account for and the target material. The materials of interest are silicon and germanium since they are the detector materials used in the SuperCDMS SNOLAB

experiment. There are many neutrino sources that could be accounted for. Here we are mainly interested in solar neutrinos, atmospheric neutrinos (produced by cosmic-ray interactions with Earth's atmosphere), and neutrinos from distant core-collapse supernovae (diffuse supernova neutrino background).

There are nine main ways for the production of solar neutrinos: *pp* neutrinos, *hep* neutrinos, ^{8}B neutrinos, ^{7}B neutrinos, ^{13}N neutrinos, ^{15}O neutrinos and ^{17}F neutrinos which all have continuous neutrino spectra as well as *pep* which has one discrete line at 1.442 MeV and ^{7}Be which has two discrete lines at 0.862 and 0.384 MeV [**10**]. The diffuse supernova neutrino background can be approximated using a thermal spectrum [**28**].

Figures 1.2 and 1.3 show the differential coherent neutrino scattering (CNS) rate as a function of recoil energy for germanium and silicon respectively. The neutrino flux, as mentioned above, comes directly from the SuperCDMS internal database. There are sixteen different neutrino spectra taken into account: *pp* (data 1 of the Figures), *pep* (data 2), *hep* (data 3), ^{7}B at 0.384 (data 4) and 0.862 (data 5) MeV, ^{8}B (data 6) ^{13}N (data 7), ^{15}O (data 8), ^{17}F (data 9), three spectra for the diffuse supernova background with effective temperatures of 8 MeV (data 10), 5 MeV (data 11) and 3 MeV (data 12), four spectra for atmospheric neutrinos representing the different types of neutrinos produced v_e (data 13), $\bar{v}_e$ (data 14), v_μ (data 15) and $\bar{v_\mu}$ (data 16). The total differential neutrino event rate is represented by data 17. Since the coherent neutrino background is known as a main background source for direct dark matter searches, these two figures will later be compared with the differential photon elastic scattering rates in Section 3.1 and Chapter 4. This will give a baseline for comparing one background source to another.

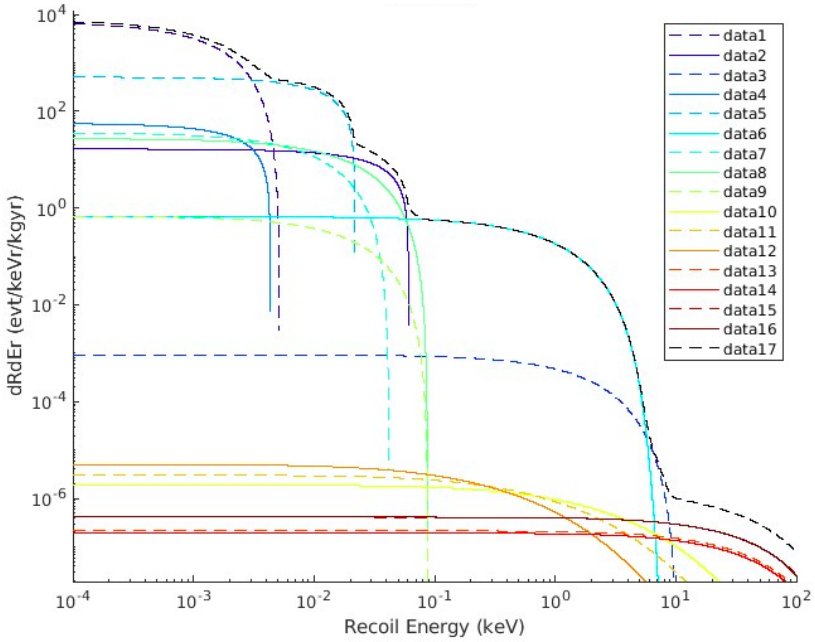

Fig. 1.2. The differential coherent neutrino scattering rate as a function of recoil energy for a germanium target. As mentioned in the text, 16 different neutrino spectra are present (data 1-16) with data 17 being the sum total.

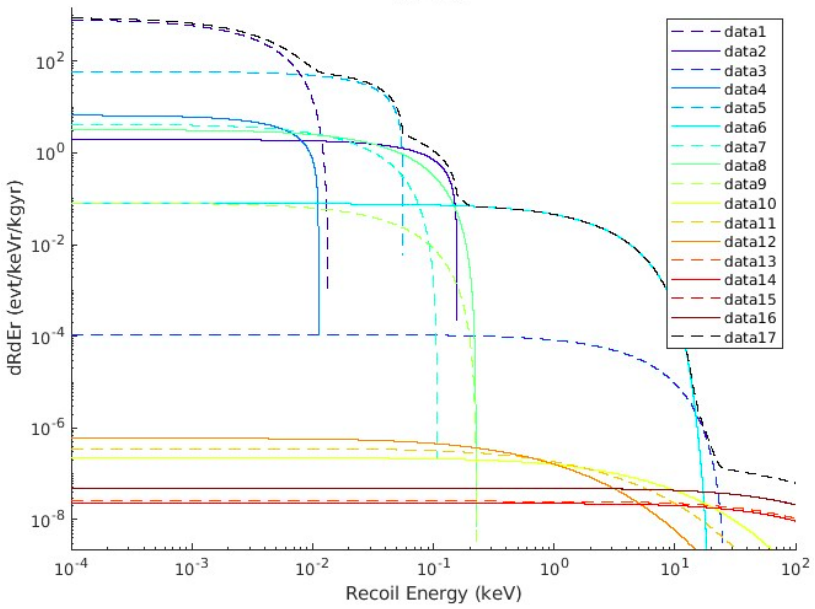

Fig. 1.3. The differential coherent neutrino scattering rate as a function of recoil energy for a silicon target. As mentioned in the text, 16 different neutrino spectra are present (data 1-16) with data 17 being the sum total.

Chapter 2

SuperCDMS SNOLAB sensitivity

SuperCDMS SNOLAB is a modern direct detection experiment with the hope of discovering Weakly Interacting Massive Particles (WIMPs) in the sub 10 GeV/c^2 mass range which could be considered dark matter. The experiment is currently under development at the SNOLAB underground science laboratory [**3**].

Many dark matter experiments looking for WIMPs have already put a strongly constraining upper limit on the WIMP-nucleon cross section for the majority of the GeV and TeV mass range. Figure 2.1 shows the upper limits set by different spin-independent elastic WIMP-nucleon scattering experiments [**13**].

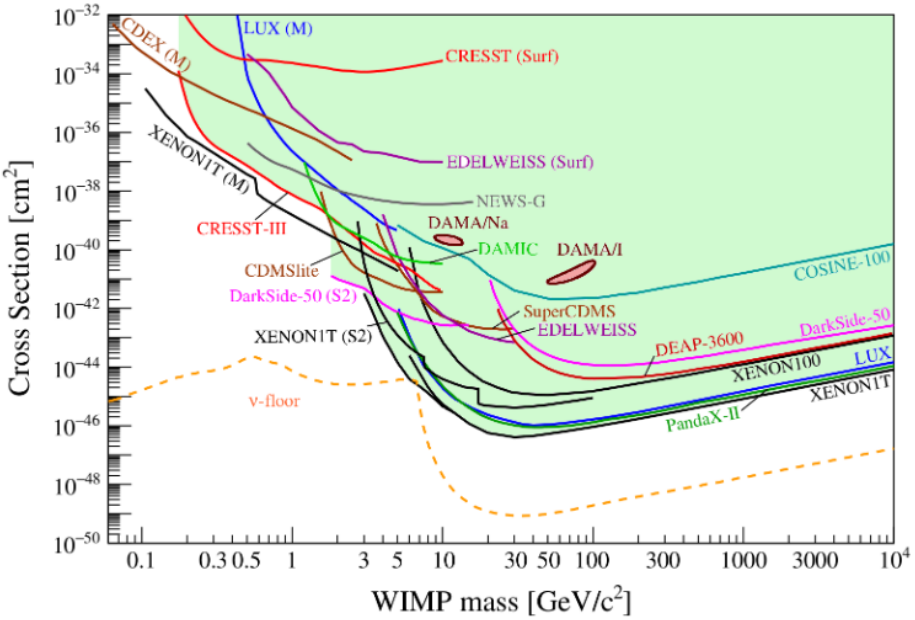

Fig. 2.1. Cross section (cm^2) as a function of WIMP mass (GeV/c^2) of past spin-independent elastic WIMP-nucleus scattering experiments using the standard parameters for an isothermal WIMP halo: $\rho_0 = 0.3$ GeV/c^2/cm^3, $v_\chi = 220$ km/s, $v_{esc} = 544$ km/s. Figure taken from Reference [**13**].

While examining Figure 2.1 a noticeable relatively high cross section upper limit has been set with respect to the neutrino floor for WIMP masses smaller than 10 GeV/c^2. A major goal of the SuperCDMS SNOLAB experiment is to decrease this upper limit set by past dark matter direct detection experiments for WIMP masses smaller than 10 GeV/c^2. SuperCDMS SNOLAB's expected upper limits on the spin-independent WIMP-nucleon cross section are shown in Figure 2.2.

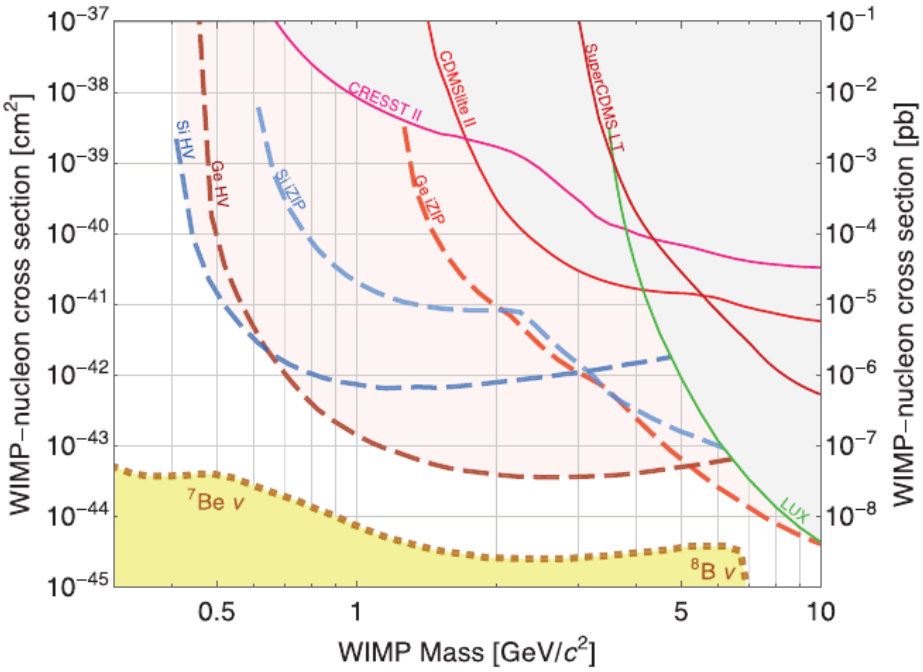

Fig. 2.2. Projected exclusion sensitivity for the SuperCDMS SNOLAB direct detection dark matter experiment. The vertical axis is the spin-independent WIMP-nucleon cross section under standard halo assumptions while the horizontal axis is the WIMP mass. Figure taken from Reference [**3**].

This section aims to give a general overview of the SuperCDMS SNOLAB experiment. This overview includes topics such as the experimental configuration, sources of background, and detector response in order to understand some parts of how the projected exclusion sensitivity of Figure 2.2 was calculated. The information presented in this section is based on Reference [**3**] unless otherwise cited.

2.1. The detectors

The sensitive part of the SuperCDMS experimental configuration will be made up of four towers each with six detectors totaling twenty-four detectors. There are two different types of detectors called HV and iZIP whose designs complement each other.

These two detector types are both cylindrical with the same dimensions (100 mm in diameter and 33.3 mm thick) and are made up of either germanium or silicon. The four

dashed lines in Figure 2.2 represent the projected exclusive sensitivity for the four types of detectors previously mentioned. The HV detectors have the ability to detect lower energy recoils compared to the iZIP. This is the main reason why the exclusion sensitivity of the HV detectors extends to lower WIMP masses when compared with iZIP detectors. This section will go over the detectors' unique sensitivity to low-energy recoils by describing the technology. Furthermore, the unique problem for coherent scattering backgrounds is that, unlike other backgrounds, they affect both the HV and iZIP detectors in similar ways leading to difficulties in discriminating these types of background events.

The differentiating features of the HV and iZIP detectors are the superconducting sensors placed on their top and bottom faces and the applied bias voltage. Although the HV and iZIP detector faces both have twelve phonon channels (six on both sides) with each channel having hundreds of superconducting sensors, their channels are arranged differently. The iZIP has two additional ionization channels which occupy the same space as the phonon channels. The operating voltage for the iZIP detectors ranges from 5 to 10 V. The iZIP's phonon channels are grounded so the operating voltages mentioned are only applied to the ionization channels. The HV detectors on the other hand are designed to operate with a bias up to at least 100 V for both the germanium and silicon detectors. Figure 2.3 shows the arrangement of the different channels for the HV and iZIP detectors.

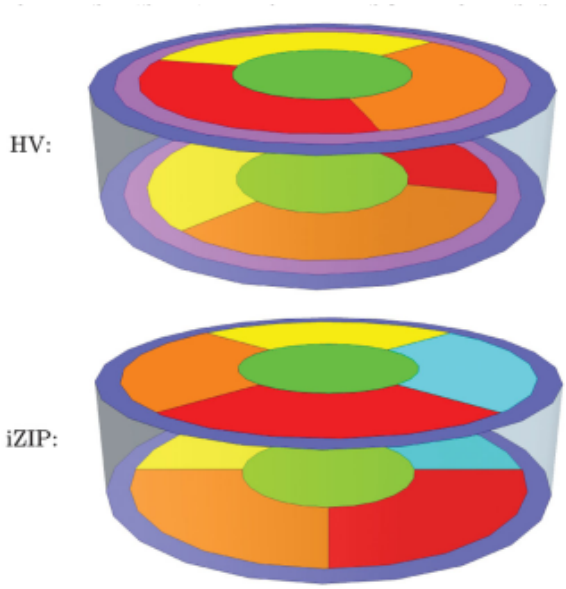

Fig. 2.3. Arrangement of the different channels for the HV and iZIP detectors where each color represents a different phonon channel. The wedge-shaped channels on the bottom surface of the HV and iZIP detectors are rotated by 60°and 45°respectively with respect to the top surface. One of the iZIP's ionization channels is interleaved with the phonon channel represented by the dark blue outer ring while the other ionization channel is interleaved with all the other phonon channels. This figure is taken from Ref [**3**].

The HV detectors' high voltage bias allows them to take advantage of the Luke-Neganov effect. This effect gives a way to amplify the phonon signal through a bias voltage. The Luke-Neganov effect happens when the recoil energy is greater than the bandgap energy which for germanium and silicon is $\epsilon_{gap} \sim 1.1$ eV and 0.67 eV respectively [**30**]. Since there is a bias voltage applied to the detectors, the charge carriers produced will create additional phonons while moving toward the biased surfaces which are called Neganov-Trofimov-Luke (NTL) phonons. Because the energy gained by the charge carriers through the bias voltage will be converted into phonon energy, we have

$$E_{ph} = E_r + n_{eh} \cdot e \cdot V \tag{2.1.1}$$

where E_{ph} is the energy of the phonons, E_r is the recoil energy, n_{eh} is the amount of electron hole pairs created, e is the charge of an electron and V is the biased voltage. The charge production can be written:

$$n_{eh} = y(E_r)\frac{E_r}{\epsilon_{eh}} \tag{2.1.2}$$

where $y(E_r)$ is the charge yield which is 1 for electron-recoils and between 0% and 30% for nuclear recoils and ϵ_{eh} is the average energy needed to create an electron-hole pair. The total phonon energy can then be written:

$$E_{ph} = E_r \left(1 + e \cdot V \cdot \frac{y(E_r)}{\epsilon_{eh}}\right). \tag{2.1.3}$$

For high enough voltages, the phonon energy is dominated by NTL phonons making it proportional to the energy gained by the charge carriers. For low voltages, the phonon energy is a mixture of both the recoil energy and the energy gained by the charge carriers. This gives the opportunity for two different modes of operation; a high voltage and a low voltage mode which are the general ideas behind the HV and iZIP detectors respectively. The low voltage mode with independent measurements of liberated charges and phonons will be able to discriminate between electron-recoils and nuclear-recoils because the charge yields for these interactions are different. While the high voltage mode is not able to discriminate between the two types of recoils, it can increase the phonon energy substantially with respect to the recoil energy leading to a detectable phonon signal for smaller recoil energies [**35**].

Due to the two different modes of operation (high and low voltage), the HV and iZIP detectors were designed in order to complement each other. The HV detectors are better for WIMP masses $\lesssim 5$ GeV/c^2 because of their high operating voltage [**2**] while the iZIP detectors are better for WIMP masses ~ 5 GeV/c^2 because of their ability to discriminate between electron-recoils and nuclear-recoils [**1**].

Once the phonons reach the faces of the detectors they need to be measured. The phonon sensors are called Quasiparticle trap-assisted Electrothermal-feedback Transition-edge sensors (QETs). These QETs need to be kept just below their superconducting temperature. When phonons reach the detectors' surfaces, they will heat up the QETs which causes a measurable spike in resistance. The greater the phonon energy, the greater the spike in resistance, giving a measurement of the phonon energy [**35**].

To summarize, the HV and iZIP detectors are designed to supplement each other's capabilities. Both detector types have the ability to detect low-energy recoils. The HV detectors can detect lower recoil energies than the iZIP detectors while the iZIP detectors can discriminate between electron and nuclear recoils. Since coherent scattering affects both of these detectors through nuclear recoils, the discrimination feature of the iZIP detectors isn't able to diminish the coherent photon scattering background signal.

2.2. Cryostat and shielding

Other than the detector and detector towers, the SuperCDMS experiment also has heavy shielding, a cryogenic system, and a seismic platform. Figure 2.4 shows the general experimental setup of the components mentioned. It is important to understand the cryostat and shielding layouts since they play an important role in determining the radiation environment for the detectors.

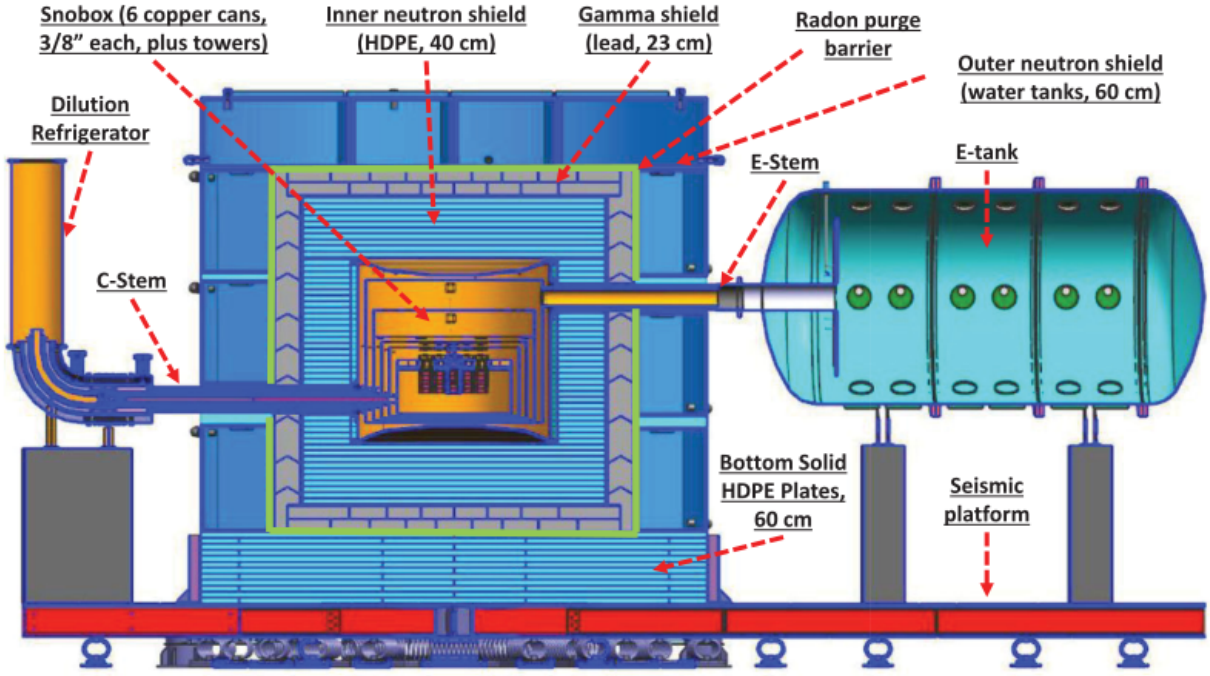

Fig. 2.4. The experimental setup of the shielding, cryogenic system, and seismic platform for the SuperCDMS SNOLAB experiment. Figure taken from [**3**].

The cold part of the setup shown in Figure 2.4 is referred to as SNOBOX which consists of six copper cans and the detector towers. Each of the copper cans are assigned to a thermal stage of the refrigerator for temperature control. The detector towers in SNOBOX are planned to be cooled to 30 mK but can go as low as 15 mK due to the dilution refrigerator which is in charge of cooling the system down and the C-stem (cryogenic stem) which conducts the heat towards the dilution refrigerator [**45**]. As mentioned in Section 2.1, this is important because the detectors' sensors need to be cooled to superconducting temperatures in order to work properly. The dilution refrigerator and the C-stem make up the main components of the cryogenic system.

The detector shielding consists of multiple parts. The innermost shielding section is a 40 cm thick layer of polyethylene that surrounds SNOBOX in order to shield the detectors from incoming neutrons. This innermost layer is surrounded by a 23 cm thick layer of lead to shield the detectors from gamma particles. Surrounding the layer of lead is a layer of aluminum which shields the inner layers previously mentioned from being contaminated by radon diffusion. The outermost layer is 60 cm thick and is made up of water tanks and polyethylene to offer extra protection from neutrons. The whole SuperCDMS experiment is set up 2 km underground, providing more shielding from cosmic radiation.

The other parts of the setup of Figure 2.4, the E-tank (electronic tank) and the seismic platform are outside the shielding. Therefore, they do not significantly affect the radiation environment of the detectors and the E-stem penetration through the shielding.

2.3. Sources of Background

As the name suggests, in order to suppress sources of background, SuperCDMS SNOLAB is being built within the SNOLAB underground science facility located in Sudbury, Ontario Canada. The SNOLAB facility was built to combine great depth (2 km) with a cleanroom environment making it ideal for sensitive experiments such as dark matter direct detection experiments. [**21**]. Even with these measures taken to minimize the sources of background, there are still a variety of sources that need to be taken into account for the SuperCDMS experiment. There are many event-producing background sources that need to be taken into account for the SuperCDMS experiment. These sources include impurities in the detector crystals, activation and contamination of the material surrounding the detectors, surface contaminants, radioactivity of the underground cavern in which SNOLAB is located and cosmic backgrounds.

Sections 2.3.1, 2.3.2 and 2.3.3 explore the radioisotopes present in the SuperCDMS SNOLAB experiment. In these sections, only radioisotopes with relatively long half-lives are considered since the materials used have a "cooling" period which would get rid of shorter-lived radioactive isotopes. It is also useful to note that since the objective of Chapter 2 is

to gain an understanding of Figure 2.2, the values mentioned in Section 2.3 will differ from more up-to-date data [**18**] used for the following chapters of the thesis.

The most important background sources for γ-ray elastic scattering are of course the ones that produce γ-rays. The radioisotopes in activated and contaminated materials mentioned in Sections 2.3.2 and 2.3.3 represent the main source of γ-rays in the SuperCDMS SNOLAB experiment. Coherent neutrino interactions mentioned in Section 2.3.9 give a baseline to compare photon elastic scattering too. The remaining sections are less important for γ-ray elastic scattering but are present to give a more complete overview of SuperCDMS SNOLAB backgrounds and the modeling behind the creation of Figure 2.2.

2.3.1. Impurities in the detector crystals

Radioactive impurities in the detector crystals are expected to be the most important source of backgrounds. The radioactive isotopes in the detector crystals are ^{3}H which can be found in both germanium (Ge) and silicon (Si) detectors, ^{32}Si which contaminates the Si detectors and ^{68}Ge its daughter isotope ^{68}Ga, ^{65}Zn, ^{73}As, ^{57}Co, ^{55}Fe, ^{54}Mn and ^{49}V which contaminate the Ge detectors [**8**]. These radioisotopes have sufficiently long half-lives to contribute to the background of the SuperCDMS experiment.

The tritium (^{3}H) atoms are produced through cosmic-ray secondaries interacting with the nuclei in germanium and silicon crystals [**8**]. ^{3}H is a β-emitter with a half-life of 12.3 years. The effect tritium has on backgrounds is modeled using production rates and activation times in Ge [**17**], Si, and a generic β-decay energy spectrum [**40**]. The production rate of the Ge (Si) detectors are taken to be 80 (125) atoms/kg/day while the concentration for the HV and iZIP detectors are 0.7 (1) and 1.5 (2) decays/kg/day respectively. The concentration of the HV and iZIP detectors is calculated using the production rates mentioned, the mass of the detector crystals, and assuming an exposure of 60 (125) days for the HV (iZIP) detectors and an underground "cooling" period of 365 days.

^{32}Si is also produced through cosmic-ray secondaries interacting with the silicon crystals [**20**] and has a half-life of around 153 years [**44**]. The ^{32}Si concentration assumed in the creation of Figure 2.2 was taken from Reference [**4**] and is taken to be 80 decays/kg/day.

All these sources produce electron recoils, largely from β-decay or Auger electrons, that iZIP detectors can nominally discriminate against.

2.3.2. Material internal activation

Materials outside of the detector crystals can also become activated through interactions with cosmic-ray secondaries leading to the production of radioisotopes with relatively long half-lives compared to the "cooling" period. The most important cosmogenic activation occurs in copper found in the detector towers and cryostat. This contamination

consists of four main radioisotopes[1]: ^{56}Co, ^{57}Co, ^{58}Co, ^{60}Co. The respective production rates (atoms/kg/day) of these isotopes are taken to be 20, 155, 143, and 181 and are taken from the sea-level rates of Reference [**14**]. Other secondary background sources for SuperCDMS activated materials are ^{46}Sc, ^{54}Mn, ^{59}Fe, and ^{48}V, Their respective production rates (atoms/kg/day) are 4.6, 19, 39 and 9.5 which are also taken from the sea-level rates of Reference [**14**] except for ^{48}V which is taken from Reference [**36**]. The contamination rate of all these activated atoms can then be calculated similarly to the tritium concentration using the mass of the atoms present and with an assumption on their exposure and "cooling" periods. Activated radioisotopes in SuperCDMS SNOLAB materials are a major source of γ-rays, making them especially important when modeling the γ-ray elastic scattering background.

Table 2.1 shows the contamination rates of the isotopes coming from activated materials. As mentioned in its caption, the creation of Figure 2.2 only accounts for the isotopes ^{57}Co, ^{58}Co, ^{60}Co and ^{54}Mn for the housings and towers while solely accounting for ^{60}Co in the cryostat cans. These approximations are done because the contamination rates for the isotopes not accounted for are at least five times lower. For future and more accurate sensitivity predictions of the SuperCDMS SNOLAB experiments, all isotopes are taken into account.

	Contamination Rates (μBq/kg)	
Isotope	Housing/Towers	Cryostat
^{56}Co	3.5	2.3
^{57}Co	62	89
^{58}Co	23	13
^{60}Co	47	90
^{46}Sc	0.88	0.62
^{54}Mn	7.9	12
^{59}Fe	2.9	0.9
^{48}V	0.76	0.25

Table 2.1. The contamination rates in μBq/kg for the radioisotopes coming from activated materials in the SuperCDMS experiment. The assumptions used are the production rates mentioned in the text, a sea-level exposure of 90 days followed by a 90 day underground "cooling" period for copper in the housings and towers and a sea-level exposure of 180 days followed by a 180 day "cooling" period for the copper cryostat cans. The contamination rates and assumptions used come from Reference [**3**] where the assumptions for the other elements are not mentioned. In the creation of Figure 2.2, only the isotopes ^{57}Co, ^{58}Co, ^{60}Co and ^{54}Mn are taken into account for the housings and towers with ^{60}Co being the only one taken into account for the cryostat.

[1]Co is the chemical symbol for cobalt

2.3.3. Material internal contamination

Instead of materials being activated by cosmic ray secondaries, radioisotopes can be introduced to the materials during the manufacturing process. The three main sources of contamination for the SuperCDMS SNOLAB materials are ^{232}Th, ^{238}U, and ^{40}K. They are unstable isotopes with relatively long half-lives of 1.40×10^{10} years, 4.468×10^{9} years, and 1.248×10^{9} years respectively [**41**]. ^{232}Th and ^{238}U have decay daughters which are measured to be in secular equilibrium. ^{40}K does not have radioactive decay daughters. In addition to these three contaminants, ^{60}Co and ^{137}Cs account for the minority of the total contamination but are also accounted for. These two radioisotopes do not have radioactive decay daughters. Table 2.2 shows the impurity concentrations (mBq/kg) used in the creation of Figure 2.2.

	Impurity concentrations (mBq/kg)				
Material	^{232}Th	^{238}U	^{40}K	^{60}Co	^{137}Cs
Copper	0.02	0.07	0.04	–	–
Cirlex	2.2	6.3	1.6	0.01	0.01
Kevlar	140	430	870	–	–
μ-metal	4.2	4.2	1.7	0.51	0.27
HDPE	1.5	0.6	1.9	0.13	0.9
Lead	0.5	0.66	7	–	–
Polypropylene	1.5	0.6	1.9	0.13	0.19
Water	1.5	0.6	1.9	0.13	0.19

Table 2.2. The assumed radioisotope impurity concentrations coming from contaminants of SuperCDMS SNOLAB materials. The impurity concentrations for copper and Lead are taken from Reference [**6**], cirlex, μ-metal, and high-density polyethylene (HDPE) are taken from Reference [**38**] and Kevlar is taken from Reference [**7**]. The impurity concentrations for polypropylene and water are assumed to be the same as HDPE as a conservative estimation.

In addition to the impurity concentrations of Table 2.2, a total emission of 0.1 mBq for ^{232}Th, ^{238}U, and ^{40}K is assigned to the "FETCard", "SquidCard", "TowerTruss" and flex cable volumes found in Figure 2.5 to account for smaller components such as screws, resistors, amongst others. Like the radioisotopes of Section 2.3.2, radioisotope contaminants in SuperCDMS SNOLAB materials are also a significant source of γ-rays. Therefore, these are important sources to account for when finding estimates on the γ-ray elastic scattering background.

2.3.4. Non-line-of-sight surfaces

The radioactive background sources mentioned are present throughout the material volumes. There are, however, background sources present solely on the material volumes'

surfaces. These surface radioisotopes accumulate through exposure to air containing dust and radon before entering SNOLAB. Generally, dust has relatively high concentrations of ^{232}Th, ^{238}U and ^{40}K while ^{222}Rn (with a half-life of 2.82 days [**41**]) can decay to ^{210}Pb which has a much longer half-life of 22.20 years [**41**] and therefore should be taken into account. ^{210}Pb has two main radioactive decay daughters: ^{210}Bi and ^{210}Po.

The analysis of surface contaminants can be separated into two categories: non-line-of-sight surfaces (surfaces without a clear line of sight to the detectors) and line-of-sight surfaces (surfaces with a clear line of sight to the detectors). This Section will talk about the former while Section 2.3.5 will be about the latter.

For non-line-of-sight contaminants, the focus is on X-rays, gammas, and neutron emissions since these are the only emissions that would be able to reach the detectors. X-rays are produced by ^{210}Pb which could reach the detectors if emitted at a close enough distance. ^{210}Bi β-decay can produce bremsstrahlung X-rays of higher energies than the ^{210}Pb X-rays. ^{210}Po goes through α decay which through interaction with ^{13}C neutrons can produce free neutrons which can reach the detectors. Therefore, the accumulation of ^{210}Pb on hydrocarbon surfaces such as polythene and HDPE are important to account for. The assumptions used for Figure 2.2, are an air exposure time of 100 days containing a ^{222}Rn concentration of 10 Bq/m^3 for surfaces inside the cryostat and 130 Bq/m^3 for the outer cryostat and shielding surfaces. This results in ^{210}Pb activities of 850 nBq/cm^2 for the inner cryostat surfaces and 11000 nBq/cm^2 for the outer cryostat and shielding surfaces. The contamination coming from the dust in the air is not accounted for in Figure 2.2 and is expected to contribute less than or similarly to the backgrounds of ^{222}Rn contamination.

Since the radioactive sources do not have a direct line of sight to the detectors and SuperCDMS SNOLAB has measures implemented to keep ^{222}Rn and dust exposure low, non-line-of-sight background sources are expected to be low and negligible for photon elastic scattering.

2.3.5. Line-of-sight surfaces

As mentioned in Section 2.3.4, line-of-sight surfaces are surfaces that have a direct line of sight to the detectors. These line-of-sight surfaces include the detector and inner surface of the copper housings. Just like in Section 2.3.4, these surfaces can get contaminated by air containing dust and ^{222}Rn where the dust can have trace amounts of radioisotopes ^{232}Th, ^{238}U and ^{40}K while the relatively short-lived ^{222}Rn (half-life of 2.82 days [**41**]) can decay into longer lived ^{210}Pb (half-life of 22.20 years [**41**]) which then accumulates on surfaces. The radioactive contaminants contained in dust are not taken into account for Figure 2.2 and therefore will not be mentioned further in this section.

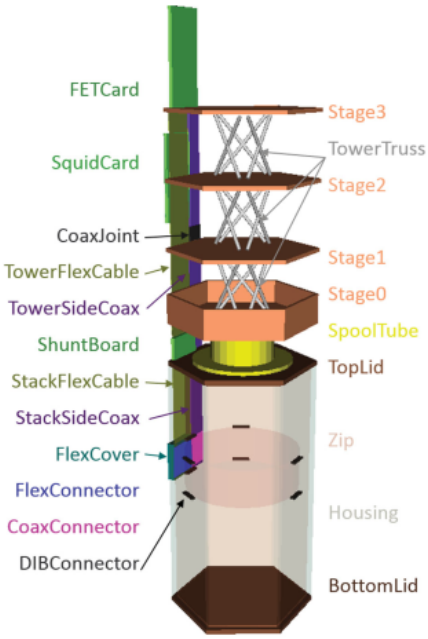

Fig. 2.5. A detailed layout of the tower mechanical support and instrumentation for one of six detectors in a tower used in the SuperCDMS SNOLAB experiment. Figure taken from [**3**].

^{210}Pb decay releases low energy β particles with an endpoint energy of ∼60 keV [**16**] and X-rays creating near-surface ER backgrounds in all detector types. ^{210}Bi β-decays with a ∼1.2 MeV endpoint energy which also creates near-surface ER backgrounds. ^{210}Po decays into a high energy (∼800 keV [**16**]) α particle which is generally outside the dark matter signal region and into ^{206}Pb which, although stable [**41**], can have enough energy to create a NR in the dark matter signal region. If the ^{210}Po decay happens on the detector surface such that the ^{206}Pb recoil is directed towards the detector surface, the full 103 keV recoil energy will be deposited into the detector. On the other hand, if the decay happens on the detector housing, the energy carried by the ^{206}Pb atom can be lowered depending on the implantation depth of the ^{210}Po parent resulting in a continuum of NR energies up to 103 keV. The assumption made for Figure 2.2 is a ^{210}Pb surface activity of 50 nBq/cm^2 for line-of-sight surfaces.

2.3.6. SNOLABs cavern environment

Sources of background coming from the underground environment itself come from naturally occurring radioisotopes present underground leading to the creation of γ-rays and neutrons which can pass through the shielding surrounding the detectors. The cavern is surrounded by rock which has been coated with a layer of shotcrete (sprayed on concrete). The floor of the cavern is made of concrete while the wall and floor have thicknesses of a few

inches. The norite rock surrounding the SNOLAB laboratory contains radioisotopes such as ^{40}K, ^{238}U, ^{232}Th and ^{222}Rn [**21**].

The γ-ray background comes from ^{40}K, ^{222}Rn decay as well as the decay chains in secular equilibrium for ^{238}U and ^{232}Th. The chances of these γ-rays reaching the detector are elevated because of the E-stem and C-stem (see Figure 2.4) penetrations through the shielding. Even then, the expected background coming from SNOLAB's cavern environment is expected to be subdominant when compared to other sources and is not included in the analysis for Figure 2.2.

2.3.7. Neutron backgrounds

The neutron background comes from the radioisotopes ^{238}U and ^{232}Th in either the cavern environment, material contamination, or radon deposition. Spontaneous fission of ^{238}U creates neutrons that can contribute to the neutron background. Another source for the neutron background comes from the alpha-emitting isotopes in the ^{238}U and ^{232}Th chains which, through α-neutron reactions, produce free neutrons that can reach the detectors. With strict radiopurity controls, at $\sim$ eV recoil energies, the backgrounds from neutrons are expected to be subdominant to coherent neutrino scattering.

2.3.8. Cosmic rays

Although SNOLAB is approximately 2 km underground, it does not completely eliminate cosmic ray background. Muons are able to pass through detectors and also create secondary particles by interacting with laboratory materials. The most important of these secondary particles are neutrons produced through spallation. The muon energy and angular distribution used to predict its contribution to backgrounds was parameterized by Mei and Hime [**39**] and uses SuperCDMS SNOLAB specific input parameters.

2.3.9. Coherent neutrino interactions

Coherent neutrino scattering represents an important background to understand, as it can almost perfectly mimic an authentic WIMP signal [**12**]. It also represents a limiting background source as explained in Section 1.3. The main source for coherent neutrino backgrounds observable by SuperCDMS is from the decay of ^{8}B at the end of the pp-III solar fusion reaction chain. For Figure 2.2, the coherent neutrino background is approximated using neutrino fluxes from Reference [**9**], the energy spectrum of ^{8}B solar neutrinos from Reference [**52**] and the scattering cross section for coherent neutrino-nucleus interactions [**24**]. Both photon elastic scattering and coherent neutrino scattering cause low-energy nuclear recoils that cannot be discriminated against using ER/NR discrimination techniques.

The coherent neutrino scattering background will be compared to the simulated photon elastic scattering background in Chapter 4.

2.4. Cuts and cross section upper limits

The upper limits set by Figure 2.2 use the method shown in Reference [**54**]. The method presented gives a 90% confidence level exclusion cross section. The sensitivity curve is calculated from post-cut background spectra and analysis thresholds.

A simulation of the spectral response for each background component mentioned in Section 2.3 is obtained. Then a radial fiducial-volume cut is made for the HV and iZIP detectors. An additional cut to the iZIP detector is made based on phonon-ionization-based depth due to its ionization channels. The iZIP detector also has an ionization yield cut which uses both types of channels, leading to excellent discrimination for rejecting ER backgrounds in the bulk. Figures 2.6 and 2.7 are respectively the HV and iZIP post-cut and pre-cut signals. The cuts made for the iZIP detectors have a greater effect on the post-cut signal than the HV detector cuts mainly due to its ER discrimination capabilities. Both figures were produced in part using the SuperSim package.

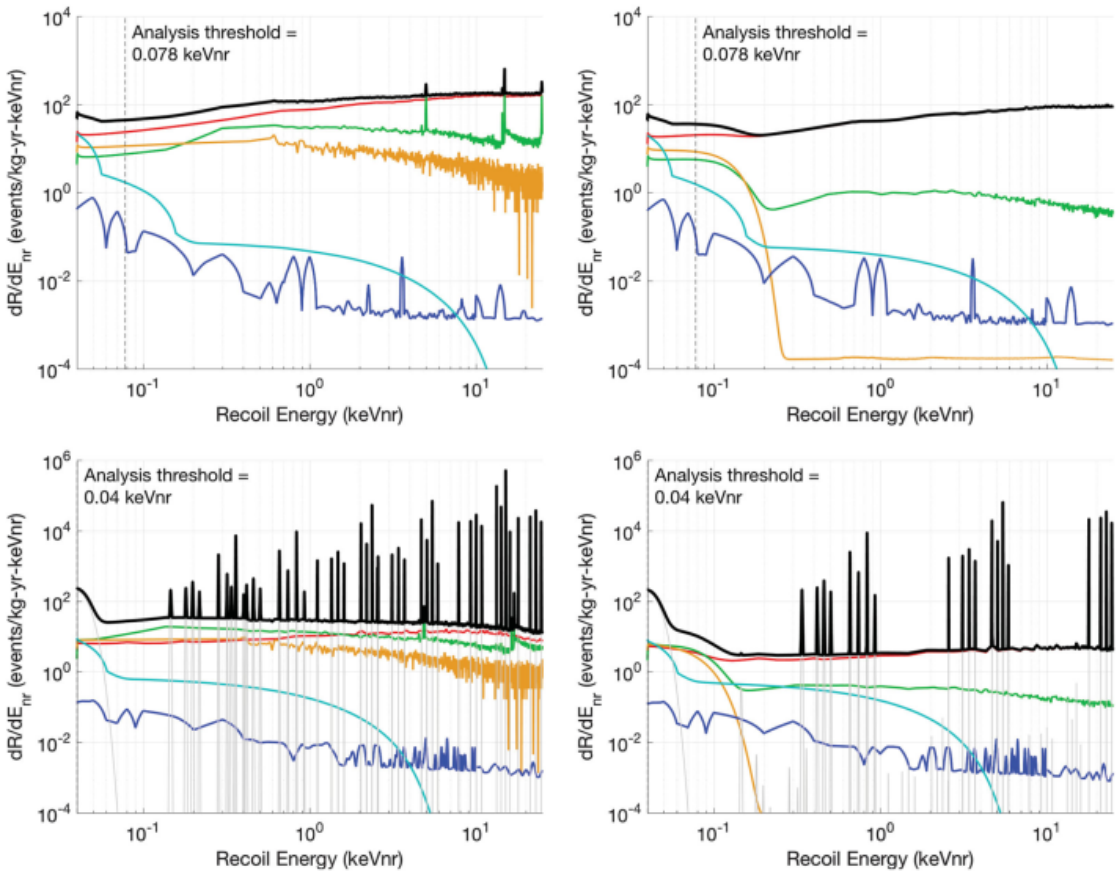

Fig. 2.6. Background spectra before (left) and after (right) analysis cuts in Si (top) and Ge (bottom) HV detectors as a function of nuclear recoil energy (keVnr). ERs from Compton γ-rays, ^{3}H, and ^{32}Si are grouped together and represented by the red line. The Ge activation lines are in grey. The surface betas are represented by the green line, surface ^{206}Pb by the orange line, neutrons by the blue line, and neutrinos by the cyan line. The black line represents the total signal. Figure taken from Reference [**3**].

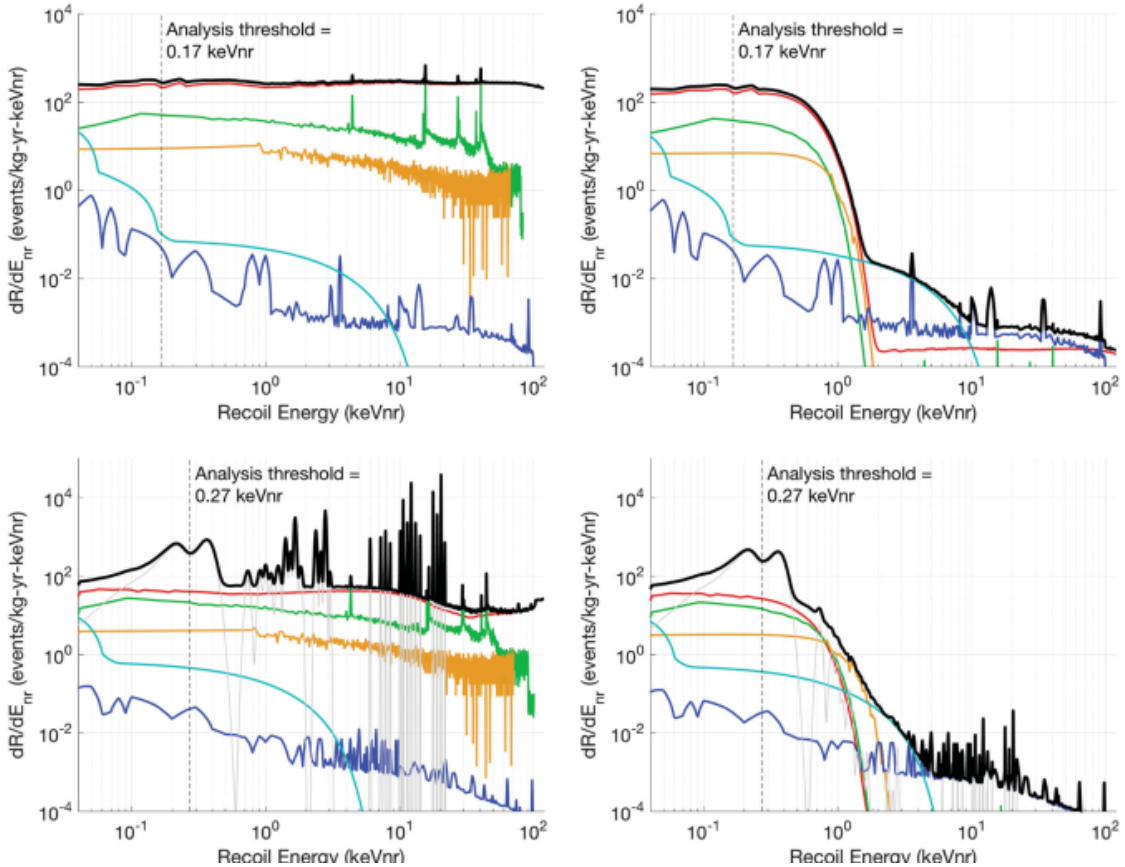

Fig. 2.7. Background spectra before (left) and after (right) analysis cuts in Si (top) and Ge (bottom) iZIP detectors as a function of nuclear recoil energy (keVnr). ERs from Compton γ-rays, ^{3}H and ^{32}Si are grouped together and represented by the red line. The Ge activation lines are in grey. The surface betas are represented by the green line, surface ^{206}Pb by the orange line, neutrons by the blue line and neutrinos by the the cyan line. The black line represents the total signal. Figure taken from Reference [**3**].

Chapter 3

Simulating γ-ray elastic and coherent scattering

Similar to sub-GeV dark matter scattering, photon elastic scattering presents itself as a nuclear recoil. This means ER/NR discrimination techniques used to suppress background signals won't work with the photon elastic scattering background. Therefore, γ-ray coherent scattering may cause a low-energy background signal that overwhelms low-threshold dark matter detectors [**47**].

The goal of this section is to motivate the simulation of γ-ray elastic scattering in the SuperCDMS simulation software called SuperSim, explain how the γ-ray elastic scattering process is implemented, mention future improvements that could be made to the simulation, and show how to use SuperSim to predict the γ-ray elastic scattering background for the SuperCDMS SNOLAB experiment.

3.1. Motivation and preliminary estimate

This section aims to motivate the use of a proper simulation of γ-ray elastic scattering backgrounds in the SuperCDMS SNOLAB experiment by building an analytic toy model to get a loose estimate of the differential elastic scattering event rate. The estimated differential event rate can then be compared with the irreducible background from neutrino scattering shown in Figures 1.3 and 1.2 for an idea of whether γ-ray elastic scattering can cause a prominent background signal.

The toy model consists of one iZIP or HV detector from Section 2.1 placed in an infinite copper sphere which is uniformly contaminated by ^{40}K radioisotopes, one of the most common backgrounds in SuperCDMS SNOLAB. As mentioned in Section 2.3, ^{40}K has a half-life $t_{1/2} = 1.248 \times 10^9$. It has two modes of decay: $\beta-$ and $\beta+$ which have branching ratios of 89.28% and 10.72% respectively. After going through $\beta+$ decay, the ^{40}K turns into the stable ^{40}Ar which then emits a 1460.8 keV γ-ray.

A narrow beam of monoenergetic photons with an incident intensity I_0, penetrating a layer of material with mass thickness x and attenuation length λ, emerges with intensity I given by the exponential attenuation law:

$$I = I_0 e^{-x/\lambda}. \tag{3.1.1}$$

The attenuation length is related to the total cross section per atom σ_{tot} by

$$\lambda = \frac{uA}{\sigma_{tot}\rho_T} \tag{3.1.2}$$

where u is the atomic mass unit, A is the relative atomic mass of the target element [**29**] and ρ_T is the target's density.

The total flux Θ that hits the detector can be approximated by

$$\Theta = \int_{all\ space} \frac{\rho_\gamma}{4\pi r^2} e^{-r/\lambda} dV \tag{3.1.3}$$

where ρ_γ is the number of γ-rays/cm^{3}yr, r is the radial distance from the position of the detector and dV is the volume element in spherical coordinates. Since we assume ^{40}K is uniformly distributed within the sphere, ρ_γ can be placed outside the integral. Integrating Equation 3.1.3 over θ and ϕ simplifies to

$$\Theta = \rho_\gamma \int_0^\infty e^{-r/\lambda} dr = \rho_\gamma \lambda. \tag{3.1.4}$$

Assuming copper has an impurity concentration of 0.04 mBq/kg [**3**] then $\rho_\gamma = 1.21$ γ-rays/cm^{3}yr. For a 1460.8 keV γ-ray in copper the total cross section $\sigma_{tot} \simeq 4.778$ barns/atom by linearly interpolating the values found in the XCOM: Photon Cross Section Database [**11**] giving $\lambda = 2.465$ cm.

The Japan Atomic Energy Agency (JAEA) [**43**] has tabulated the solid angle differential cross section $d\sigma/d\Omega$ of elements with atomic number $1 \leq Z \leq 99$. The solid angle element can be written as $d\Omega = \sin(\theta) d\phi d\theta$. A change of variables is needed to get the differential cross section $d\sigma/dE_r$. Similar to the derivation of Equation 1.1.7, a photon with energy E_γ getting scattered by a target mass m_T at an angle θ will deposit a recoil energy

$$E_r = E_\gamma \left(1 - \frac{1}{1 + E\gamma/(m_T c^2)(1 - \cos(\theta))}\right). \tag{3.1.5}$$

Using this with the fact that σ does not depend on ϕ, a change of variables yields

$$\frac{d\sigma}{dE_r} = \frac{d\sigma}{d\Omega} 2\pi \left(\frac{E_\gamma(1 - \cos(\theta)) + m_T c^2)^2}{E_\gamma^2 m_t c^2}\right) \tag{3.1.6}$$

which is the relativistic version of the formula found in the Robinson paper [**47**].

Using Equation 1.1.1 in conjunction with the values mentioned previously, Equation 3.1.6 and the differential cross section values tabulated by Omer and Hajima from JAEA [**43**], the differential rate as a function of recoil energy can be found for a given target. Figure 3.1 shows the differential event rate as a function of recoil energy for germanium and silicon detectors. Comparing the toy model's differential rate to the CNS differential rate of Figures 1.2 and 1.3 shows that the elastic scattering of γ-rays may have background effects similar to the neutrino background for sub-eV scale nuclear recoils in silicon and germanium. When compared to Figure 1.1, the toy model shows that the γ-ray differential rate is most likely higher than the dark matter differential rate for sub-eV recoils in silicon and germanium. For a dark matter mass smaller than $10\text{GeV}/c^2$, the differential dark matter rate should decrease, giving greater importance to the understanding of the backgrounds caused by γ-ray coherent scattering. Like the neutrino differential rate calculated in Section 1.3, elastic scattering of γ-rays is a purely nuclear interaction and therefore cannot be discriminated against using the iZIP's ionization channels mentioned in Section 2.4.

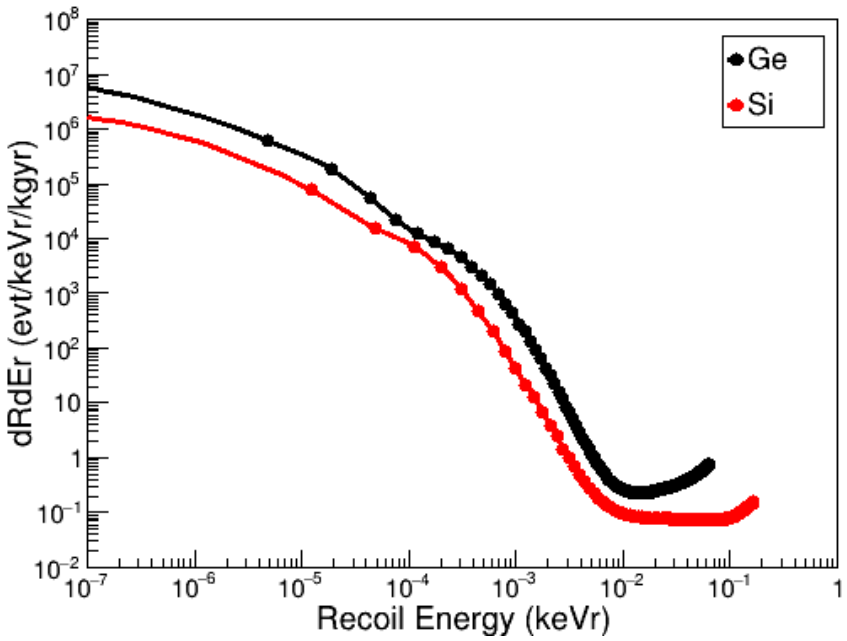

Fig. 3.1. Differential rate as a function of nuclear recoil energy for a germanium (black) or silicon (red) target inside an infinite copper sphere with a contamination rate of 0.04 mBq/kg.

3.2. SuperSim and Geant4

SuperSim is a C++ toolkit used to model geometry, physics, background sources, and more, for the SuperCDMS collaboration. It is based on Geant4 which is a toolkit used for

simulating the passage and interactions of radiation through matter. All SuperSim simulations in this thesis are based on Geant4 version 10.7.3.

Geant4 is made to be easily expanded upon due to its modular nature. It includes geometries, physical models, and more. Geant4 implements these models by organizing them into physics lists. Geant4 has many physics lists to choose from, some of which are specialized for electromagnetic interactions, high-energy physics, amongst others. The default physics list for low-energy background simulations in SuperSim is the Shielding physics list which is provided by Geant4. This physics list includes models for radioactive decay, electromagnetic interactions, and much more. SuperSim has its own set of modular code to simulate SuperCDMS specific decays, geometry, radioisotopes, and more. SuperSim even extended the Geant4 code to simulate the phonon and charge transport in semiconductor crystals [**32**]. SuperSim also provides a set of macro commands to easily customize the simulation. Although SuperSim does simulate many types of physical interactions it does not account for all γ-ray elastic scattering processes.

3.3. γ-ray elastic and coherent scattering

In the literature, elastic scattering and coherent scattering are often used interchangeably in relation to certain types of scattering mechanisms despite being defined differently. Elastic scattering is defined as a scattering process in which the target's and projectile's energies are unchanged in the center of mass frame. In other words, there is no energy transfer between the two objects. It should be noted, through conservation of energy and momentum, that there is always some energy transfer after a scattering event. Therefore, elastic scattering is an approximation where it is assumed that the initial and final energy of the photon and target are unchanged. This is a valid approximation for low energy photons (when $\hbar w << m_T c^2$). Coherent scattering refers to the fact that a cross section can only be defined for a process corresponding to observable initial and final states. An observable initial and final state may have multiple indistinguishable processes. In this case, these processes can be described by scattering amplitudes, each related to a single process that can produce the transition between the measured initial and final states. These amplitudes must therefore be squared only after being added up [**19**]. Since all scattering mechanisms mentioned in this section are both elastic and coherent across the atom, the terms will be used interchangeably.

There are multiple mechanisms for which γ-rays scatter elastically with a target material. These mechanisms include nuclear Thomson scattering, Rayleigh scattering, and Delbrück scattering. These three mechanisms respectively correspond to the scattering of photons by a target's nucleus, electron, and electric field. There is a fourth mechanism called nuclear resonance scattering that JAEA doesn't consider as its largest component, from giant dipole

resonance, is only important above 5 MeV [**43**]. I do not implement nuclear resonance scattering in this work.

This section will go over the methods used for the *G4JAEAElasticScatteringModel* which is a Geant4 electromagnetic model for γ-ray elastic scattering physics [**43**]. It will also briefly cover the physical models used by the *G4JAEAElasticScatteringModel* to get the scattering amplitudes of nuclear Thomson, Rayleigh, and Delrück scattering and how to combine these scattering amplitudes to get the differential cross section for elastically scattered photons.

3.3.1. Coherent scattering differential cross section

The coherent scattering differential cross section can be written as a function of the coherent scattering amplitude A

$$\frac{d\sigma}{d\Omega} = |A|^2 \tag{3.3.1}$$

where the coherent scattering amplitude A is the sum of the individual scattering amplitudes for each coherent scattering mechanism. Therefore,

$$A = A^R + A^T + A^D + A^N \tag{3.3.2}$$

where R, T, D, and N stand for Rayleigh, nuclear Thomson, Delbrück, and nuclear resonance respectively. Each of these individual scattering amplitudes can be expressed as having two components, one in the direction of the scattering plane $A_{||}$ and the other perpendicular to the scattering plane $A_{\perp}$. The scattering plane is defined as the plane which holds both the momentum and polarization vectors of the incident photon. For unpolarized light, the differential cross section is obtained by averaging over all incident and scattered photon polarizations [**43, 31**] leading to:

$$\frac{d\sigma}{d\Omega} = \frac{1}{2}\left(|A_{||}|^2 + |A_{\perp}|^2\right). \tag{3.3.3}$$

The next section will explain how to calculate the individual scattering amplitudes A^R, A^T, and A^D.

3.3.2. Scattering amplitudes

There are many ways to approximate scattering amplitudes. This section will focus on the ones used by Omer and Hajima [**42**] for their implementation of Thomson, Rayleigh, and Delbrück scattering in Geant4 called *G4JAEAElasticScatteringModel*.

The simplest scattering amplitude to obtain is for nuclear Thomson scattering which is represented by

$$A_{||}^{T} = -\frac{r_0 Z^2 m_e}{m_T}, A_{\perp}^{T} = -\frac{r_0 Z^2 m_e}{m_T}\cos(\theta) \tag{3.3.4}$$

where r_0 is the classical electron radius, m_T is the target nucleus mass, m_e is the electron mass, θ is the scattering angle and Z is the target's atomic number [**43**]. This is the low energy limit of Compton scattering assuming $\hbar w << m_T c^2$.

There are three main ways to compute the differential cross section of Rayleigh scattering: the form factor approximation, anomalous scattering factors for forward-angle scattering, and the second-order S-matrix element. Out of these three methods, the second-order S-matrix element method is the most computationally intensive and accurate of the three. In particular, we are most interested in non-forward scattering angles. Both the form factor approximation and anomalous scattering factors for forward-angle scattering are contained within the second-order S-matrix element [**34**]. This is the method used for the *G4JAEAElasticScatteringModel*.

Since Rayleigh scattering is the process where a photon is scattered by an atomic electron, for a precise model of the scattering, one can obtain the individual scattering amplitudes for a photon to scatter off each atomic electron separately. This can be written as

$$A^R = \sum_{\mathrm{i}} A_i^R \tag{3.3.5}$$

where A_i^R is the scattering amplitude of the incident photon scattering off of the i^{th} electron. This is another reason Rayleigh scattering is considered to be coherent. One can obtain the individual amplitudes A_i^R using an S-matrix calculation. For an initial state $|\phi_i\rangle$ and final state $|\phi_f\rangle$, the S-matrix is defined as

$$|\phi_i\rangle = S\,|\phi_f\rangle \tag{3.3.6}$$

where the S-matrix element S_{fi} can be expressed as

$$S_{fi} = \langle\phi_f|S|\phi_i\rangle\,. \tag{3.3.7}$$

For some interaction V, which is responsible for the scattering, the perturbation expansion for the S-matrix is

$$S = S^{(0)} + S^{(1)} + S^{(2)} + ... = 1 - i\int_{-\infty}^{\infty} dt_1 V(t_1) + (-i)^2 \int_{-\infty}^{\infty} dt_1 \int_{-\infty}^{t_1} dt_2 V(t_1)V(t_2) + ... \tag{3.3.8}$$

[**19**] where t_1 is the time the photon is absorbed (emitted) and t_2 is the time the photon is emitted (absorbed) in the Feynman diagram found in Figure 3.2 (3.3).

The Rayleigh scattering amplitudes used for the *G4JAEAElasticScatteringModel* in Geant4 are taken from the Rayleigh scattering database (RTAB) which were calculated

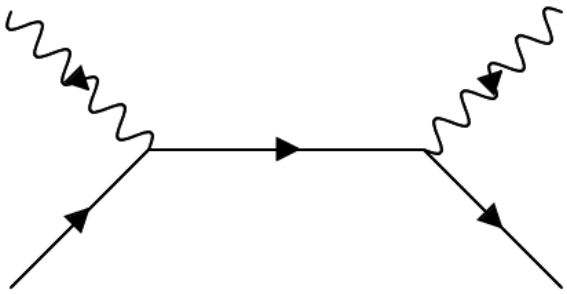

Fig. 3.2. The absorption first, two vertex Feynman diagram contribution to the $S^{(2)}$. From left to right, the first vertex represents the moment when $t = t_1$ while the second vertex represents the moment when $t = t_2$.

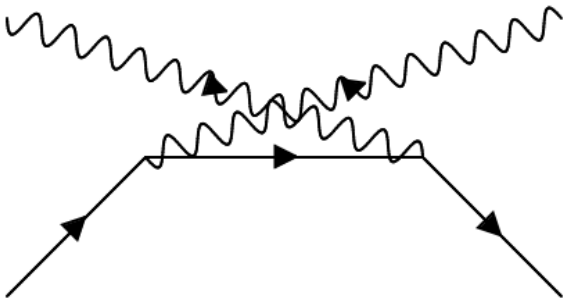

Fig. 3.3. The emission first, two vertex Feynman diagram contribution to $S^{(2)}$. From left to right, the first vertex represents the moment when $t = t_1$ while the second vertex represents the moment when $t = t_2$.

using the second-order S-matrix element [**34**]. The RTAB data used contains 56 energy points from 54.3 eV to 2.754 MeV each with 97 angular points with a greater concentration of them being for the low energies (below 10 keV) and low scattering angles (less than 10°) [**43**].

Although Delbrück scattering can be said to be the process of an incident photon elastically scattering off of the electric field of an atom, a more precise explanation is the scattering of an incident photon by virtual electron-positron pairs created in the atom's nucleus field. The real part of A^D is related to the vacuum polarization while the imaginary part is related to the absorptive process of pair production [**19**]. The Delbrück scattering amplitudes used by the *G4JAEAElasticScatteringModel* in Geant4 are taken from Reference [**23**]. These scattering amplitudes are calculated through the lowest-order Born approximation which leads to amplitudes that scale as $Z^2\alpha^3$, where Z is the atomic number of the target and α is the fine-structure constant. See Reference [**27**] for a detailed explanation of the Born approximation.

The Delbrück scattering amplitudes used have 13 energy points from 0.225 MeV to 2.754 MeV. Each of these energy points has 10-12 angular points with some starting at 1° and others ending at 175°. The 0° angular point for each energy point is calculated using the optical theorem where the scattering amplitude only depends on the energy of the incident photon [**48**] [**43**].

These three scattering processes are important for different energy and scattering angle ranges. For atoms with large Z, the Rayleigh scattering amplitudes dominate. For atoms with smaller Z, the nuclear Thomson amplitude starts to dominate in the back-scattering region. Rayleigh scattering also dominates for incident photon energies less than 1 MeV while for higher energies, its contribution is mainly for small scattering angles. Nuclear Thomson and Delbrück scattering amplitudes have very minute effects when the incident photon energy is less than 100 keV while when the photon energy increases, the nuclear Thomson and Delbrück amplitudes become important for all but small scattering angles [**19**]. For these reasons, the correct modeling of all three elastic scattering mechanisms is critical to accurately modeling backgrounds for dark matter direct detection.

3.4. G4JAEAElasticScatteringModel

The *G4JAEAElasticScatteringModel* is a subclass of the *G4VEmModel* which is a virtual class used to implement electromagnetic physics models in Geant4. This section will go over the specifics of how this electromagnetic model is implemented. The information in this section was taken from Reference [**43**] unless otherwise stated.

3.4.1. Data files

As mentioned in Section 3.3, the scattering amplitude data used by Omer and Hajima [**42**] [**43**] in their implementation of the *G4JAEAElasticScatteringModel* was taken from the RTAB [**34**] (for Rayleigh amplitudes) and Reference [**23**] (for Delbrück amplitudes) while the nuclear Thomson amplitudes are taken from Equation 3.3.4. The Rayleigh and Delbrück data sets were then interpolated to get higher resolution data. The interpolation was first made on the scattering angle θ using 721 angular points homogeneously representing the whole angular range $0° \leq \theta \leq 180°$. Another interpolation was then performed on the incident photon energy E_γ with 300 energy points distributed evenly over the energy range of 10 keV $\leq E_\gamma \leq 3$ MeV. This results in 721 (angular points) by 300 (energy points) by 4 (the $A_{||}$, $A_\perp$ scattering amplitudes, each with a real and imaginary component) by 99 (99 elements) data points for both Delbrück and Rayleigh scattering amplitudes. The four scattering amplitude components for each process (nuclear Thomson's imaginary components are all zero) are then coherently added together to get the total differential scattering amplitude for γ-ray

elastic scattering. Figures 3.4 and 3.5 shows the interpolation overlaid with the original data for Rayleigh and Delbrück scattering, respectively.

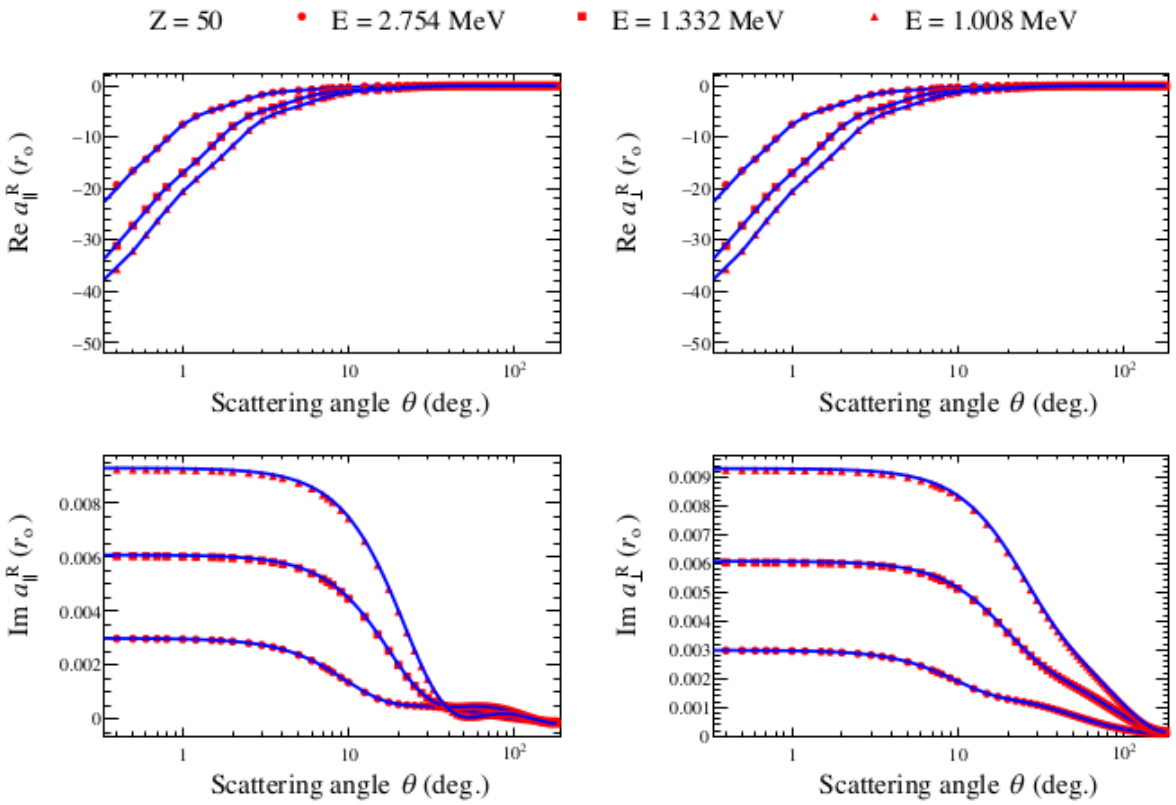

Fig. 3.4. Rayleigh scattering amplitudes from the RTAB data points superimposed with the interpolation points for a target material of atomic number 50 and three incident photon energies. The RTAB data is represented by the red points while the interpolation is represented by the blue lines. Figure taken from Reference [**43**]

In Geant4 the total cross section of a physical process is compared against all other valid physical processes to decide which will take place. Therefore, it is important to know the total cross section for each type of atom. After the interpolation of scattering angles is done, the total cross section can be computed by integrating over all angles for each photon energy and element.

99 data files are needed to run the *G4JAEAElasticScatteringModel* on Geant4. Each file contains the total differential scattering amplitude data points for one of the 99 elements ($1 \leq Z \leq 99$) for which this physical model is compatible. To decrease the size of the files and the run time of simulations that use this model, the angular data points were reduced from 721 to 181 distributed evenly over the range $0 \leq \theta \leq 180$. The number of energy data points per element remains at 300. This leads to each file having $300 + 300 \cdot 181 \cdot 4$ = 217500 data points (the total cross section for each energy point, 181 angular points for each energy, and scattering amplitude component). The total number of data points stated

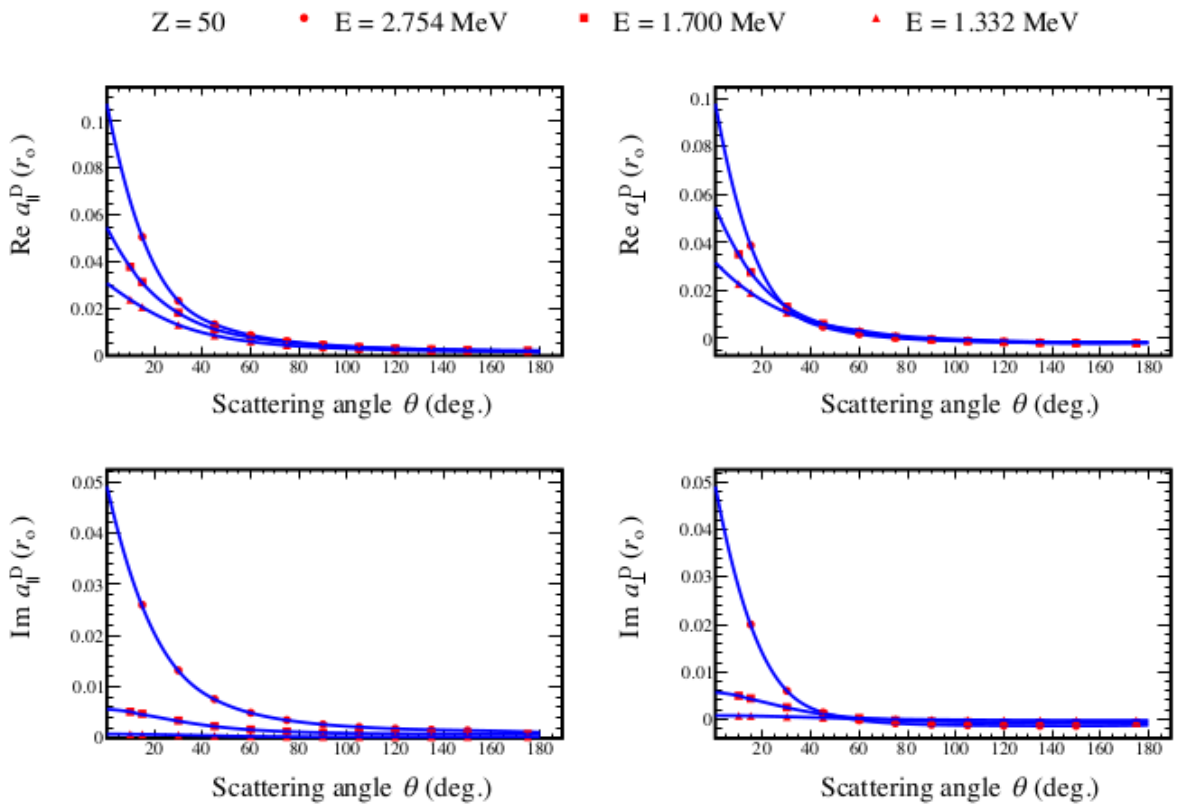

Fig. 3.5. Delbrück scattering amplitudes for the original data points taken from Reference [**23**] superimposed with the interpolation points for a target material of atomic number 50 and three incident photon energies. The original data is represented by the red points while the interpolation is represented by the blue lines. Figure taken from Reference [**43**]

in this paragraph differs from the one mentioned by Omer and Hajima [**43**] [**42**] because the file structure has changed since their publications.

3.4.2. Important functions

There are three main functions that are important in understanding how the *G4JAEAElasticScatteringModel* works. These functions are called *ReadData*, *ComputeCrossSectionPerAtom*, and *SampleSecondaries*.

The *ReadData* function is in charge of reading the data files and preparing them for use in the simulation. As mentioned in Section 3.4.1, the data file structure has changed, therefore some parts of the *ReadData* function have also been changed. Explanations on the implementation of the *ReadData* function will differ from Omer and Hajima [**43**]. Two global one-dimensional arrays (over atomic numbers 1 to 99) called *ES_Data* and *dataCS* are created in the model's header file so that they can be accessed by all class functions. The *ES_Data* array holds values from the data file while the *dataCS* array creates a spline

interpolation of the total cross section versus the incident photon energy using the stored values.

The simulation calls the *ComputeCrossSectionPerAtom* function when it needs to know the cross section of the physics process. *ComputeCrossSectionPerAtom* uses the spline interpolation feature of the objects stored in the global variable *dataCS* to return the total elastic scattering cross section for an incident photon energy and material.

The role of the *SampleSecondaries* function is to implement changes on the particles affected by the process. The function uses the energy of the incident photon and the atomic number of the target material to know which of the vectors contained in *ES_Data* to use. If the material is made up of multiple elements, it uses the Geant4 function *SelectRandomAtom* to pick the target element. Since the elastic scattering amplitude data is made up of 10 keV energy bins, the function will round the incident photon energy to the closest available energy bin within 5 keV. An array representing the differential cross section distribution will be created using Equation 3.3.3 in conjunction with the appropriate scattering amplitudes relevant to the rounded energy. Once the differential cross section distribution is created, an inverse transform sampling method is used to get the scattered photon direction. The inverse transform method creates a cumulative distribution function (CDF). Then, the CDF and a uniform random number generator are used together in order to get the scattering angle. After the scattering angle is found, the azimuth is uniformly sampled. The function then appropriately changes the direction of the incident photon.

The *G4JAEAElasticScatteringModel* is not compatible with polarized photons. If the incident photon is polarized, the function returns without implementing any changes and lets the user know an error had occurred. The model does not scatter photons below 10 keV, causing those photons to be locally absorbed instead. This 10 keV cutoff is well below the energy of photons expected to contribute to γ coherent scattering backgrounds.

3.4.3. Problems with the model

A few problems emerge when analyzing the code and data files of the *G4JAEAElasticScatteringModel*. In the *SampleSecondaries* function, the code doesn't account for a change in variables from solid angle Ω to the scattering angle θ. Also, the differential cross sections obtained using the data files do not match the documented differential cross sections reported by the creators of this model [**43**].

According to the documentation [**43**], the differential cross sections obtained through the data files are in units of barns/steradians and are tabulated as a function of θ in degrees. As mentioned in Section 3.4.2, the *SampleSecondaries* function uses the differential cross section data points with an inverse transform sampling method in order to find θ. In this process, the differential cross sections need to be converted from $d\sigma/d\Omega$ to $d\sigma/d\theta$ by multiplying the

differential cross section distribution by a factor of $2\pi \cdot \sin(\theta)$. Since this is not done, the scattered photon's final state is not accurate. This causes a serious problem when obtaining the differential scattering rate as the scattering angle translates directly into the recoil energy measured by the detectors as shown in Equation 1.1.5.

Although the *ReadData* function and data file structure were changed, there is no mention of the data itself being changed. When comparing the differential scattering amplitudes of the simulation with the ones mentioned in the *G4JAEAElasticScatteringModel* report [**43**], they differ substantially. It is worth mentioning that the total scattering cross section has not been changed and agrees with the documentation and other sources [**15**] [**11**]. Table 3.1 compares some of the uranium differential cross sections from the JAEA documentation [**43**] with the ones obtained using the files for a 40 keV incident photon. These differential cross sections differ by two orders of magnitude. If all differential cross section data points for a given energy were scaled by the same factor, it wouldn't affect the simulation since a normalization occurs in the *SampleSecondaries* function. However, as shown in Table 3.1 this is not the case, and further investigation is required.

Angle (deg)	Documentation (b/st)	Data (b/st)	Quotient
1	6.58E+02	1.64E+04	24.92
2	6.50E+02	1.58E+04	24.3
3	6.28E+02	1.50E+04	23.88
4	5.98E+02	1.42E+04	23.75
180	9.59E+00	2.41E+02	25.13

Table 3.1. Comparison of uranium differential cross section (b/st) as a function of scattering angle (deg) for an incident photon energy of 40 keV. The second column shows the values mentioned in the model's documentation [**43**], and the third column shows the values obtained in the manner implemented by the *G4JAEAElasticScatteringModel* code. The fourth column is the quotient of the third and second columns.

3.5. CDMSJAEAElasticScatteringModel and future improvements

Another problem with the *SampleSecondaries* function when it comes to dark matter direct detection searches is that it treats the collision as elastic. Since the *G4JAEAElasticScatteringModel* does not deposit energy into the target, it cannot be used to get an estimate on backgrounds. For this reason, a SuperSim version of the model was made called *CDMSJAEAElasticScatteringModel*. In this electromagnetic model, the same functions are implemented but the energy transferred by the incident photon to the target is taken into account. At the end of the *SampleSecondaries* function implemented in

SuperSim, the transferred energy is calculated using Equation 3.1.5 and is then deposited into the target.

Although the current *CDMSJAEAElasticScatteringModel* is expected to give a good approximation of the total photon elastic scattering rate (since the total cross section data points were found to be accurate), the same cannot be said for the differential rate. For future versions of the *CDMSJAEAElasticScatteringModel*, the problems mentioned in Section 3.4.3 should be fixed. Specifically, in the process of finding the scattering angle in the *SampleSecondaries* function, the change of variables needs to be accounted for and the scattering data used for the model should be investigated further in order to validate the model.

Chapter 4

The simulation

The simulation builds the whole SuperCDMS SNOLAB geometry using SuperSim. Due to the long computation time for simulating every background source in all SuperCDMS SNOLAB geometries, the only simulated background sources are the ^{60}Co and ^{232}Th isotopes present in the detector housing. The housing as the source for particle decay was chosen because it is the closest geometry to the detectors other than the detectors themselves. The ^{60}Co and ^{232}Th isotopes were chosen since they represent two of the main γ-ray sources coming from the housing. These two isotopes in the housing are expected to account for less than 10% of photons that reach the detector. The contamination rates used in the simulation are the most recent estimates and come from internal SuperCDMS data [**18**]. The simulation of ^{60}Co and ^{232}Th in the housing were run separately. For each simulation, a year's worth of decays were simulated for each source with all default SuperSim physics processes active on top of the *CDMSJAEAElasticScatteringModel*. The photon elastic scattering process was biased by multiplying the total cross sections by a factor of 1000 in order to get more statistics on the photon elastic scattering rate.

The simulation outputs all simulated data into a *.root* file. The file contains data on any interaction which deposited energy into the detector throughout the simulation. A total of 6743878 and 7145606 energy deposits came from photon elastic scattering for ^{232}Th and ^{60}Co, respectively. Dividing by the biasing factor of 1000 and the total mass of all detectors present gives $\sim$ 109 and $\sim$ 115 elastically scattered photons per year per kilogram respectively for the ^{232}Th and 60 radioisotopes found in the housing. Implementing a recoil energy cutoff of 1 eV gives $\sim$ 0.02 events kg^{-1} year^{-1} for the housing's ^{60}Co and ^{232}Th radioisotopes. Figure 4.1 shows the differential rate (events keV^{-1} kg^{-1} year^{-1}) as a function of recoil energy (keV) after accounting for the biasing of the process.

In order to compare the photon elastic scattering differential rate with the dark matter and coherent neutrino scattering differential rates of Figures 1.1, 1.2, and 1.3, the simulation data was also split up between the silicon and germanium detectors. It should be noted that

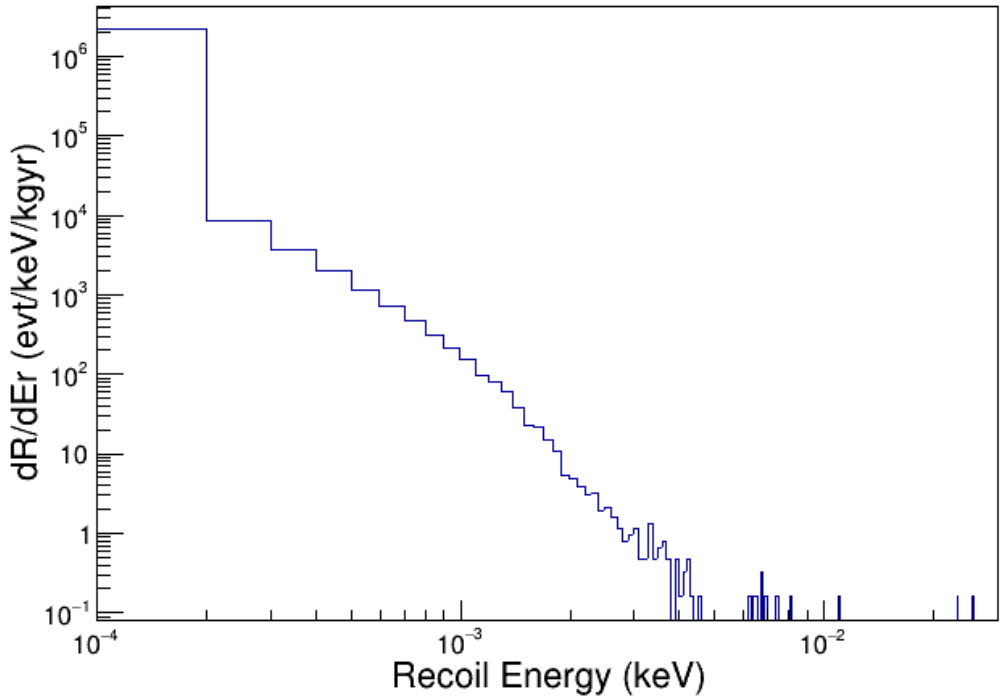

Fig. 4.1. Photon elastic scattering differential rate (events keV^{-1} kg^{-1} year^{-1}) as a function of recoil energy (keV). Data from simulating the entire SuperCDMS SNOLAB geometry using ^{60}Co and ^{232}Th inside the housing as a source. The photon elastic scattering differential rate for all SuperCDMS SNOLAB background sources is expected to be over one order of magnitude greater than shown. The histogram has 300 bins evenly distributed over the range of 0 to 0.03 keV.

there are 42 germanium detectors compared to 6 silicon detectors, so the expected number of simulated scattering interactions in each are dissimilar.

The silicon and germanium detectors have a total rate of 667972 and 13221512 energy deposits from the photon elastic scattering process, respectively. Dividing by the biasing factor of 1000 and the total mass of the detectors gives ~ 183 and ~ 226 elastically scattered photons per year and kilogram respectively for the silicon and germanium detectors. Implementing a cutoff recoil energy of 1 eV gives ~ 0.01 and ~ 0.035 events kg^{-1} year^{-1} for silicon and germanium, respectively. Figures 4.2 and 4.3 show the simulated differential elastic scattering rates for germanium and silicon superimposed with their respective differential CNS rate from Section 1.3.

All rates and differential rates presented for germanium and silicon detectors in this chapter can be approximated to be at least one order of magnitude higher. This is due to the two isotopes in the housing accounting for less than 10% of all γ-rays which reach the detectors. Since polarized photons are not compatible with the *CDMSJAEAElasticScatteringModel*, the total rates mentioned in this chapter can be seen as lower bounds. Comparing

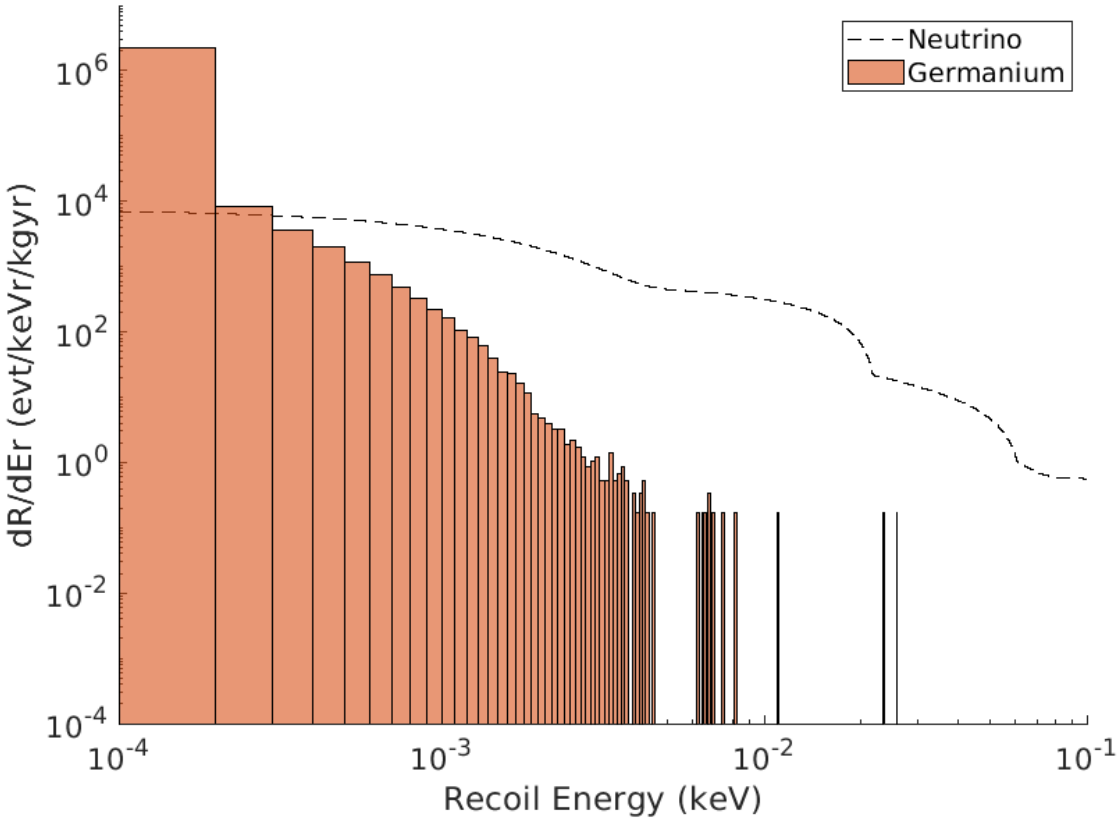

Fig. 4.2. Photon elastic scattering (bins) and total CNS (line) differential rate (events keV^{-1} kg^{-1} year^{-1}) as a function of recoil energy (keV) for germanium. Data from simulating the entire SuperCDMS SNOLAB geometry using ^{60}Co and ^{232}Th inside the housing as a source. The photon elastic scattering differential rate for all SuperCDMS SNOLAB background sources is expected to be over one order of magnitude greater than shown. The histogram has 300 bins evenly distributed over the range 0 to 0.03 keV. The CNS differential rate accounts for all CNS sources mentioned in Section 1.3.

the differential rates of Figures 4.2 and 4.3 to the toy model differential rate shown in Figure 3.1, it is clear that there is not enough data in order to replicate the higher recoil energy tail. More simulated primary particles are needed in order to smooth out the histogram at higher recoil energies.

Due to issues with the data files and the *SampleSecondaries* function mentioned in Section 3.4.3, consideration should be taken when comparing the photon elastic scattering differential rate to the CNS and dark matter scattering differential rates. Figures 4.2 and 4.3 show that the γ-ray elastic scattering differential rate above 1 eV ranges from 1-2 and 2-4 orders of magnitude below the CNS differential rate for silicon and germanium, respectively. Since these data consider less than 10% of γ-rays reaching the detectors, the γ-ray elastic scattering differential rate above 1 eV from all SuperCDMS background sources, are estimated to be

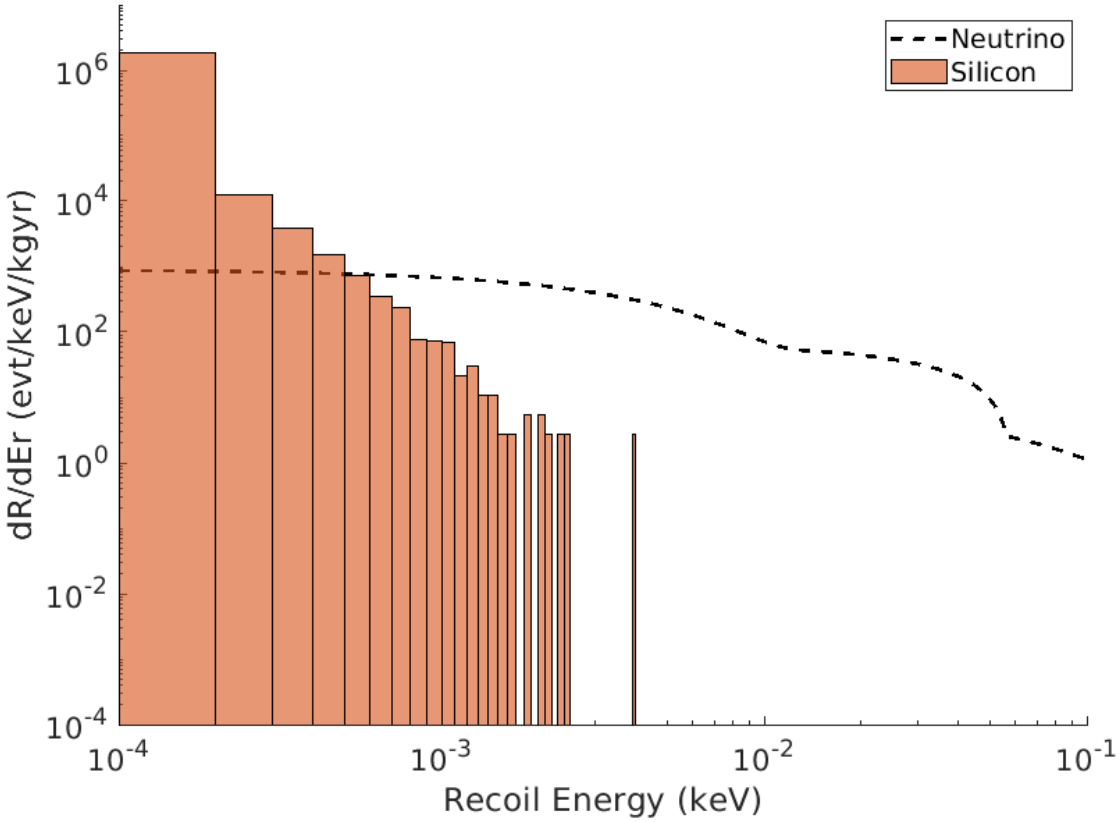

Fig. 4.3. Photon elastic scattering (bins) and total CNS (line) differential rate (events keV^{-1} kg^{-1} year^{-1}) as a function of recoil energy (keV) for silicon. Data from simulating the entire SuperCDMS SNOLAB geometry using ^{60}Co and ^{232}Th inside the housing as a source. The photon elastic scattering differential rate for all SuperCDMS SNOLAB background sources is expected to be over one order of magnitude greater than shown. The histogram has 300 bins evenly distributed over the range 0 to 0.03 keV. The CNS differential rate accounts for all CNS sources mentioned in Section 1.3.

0-1 and 1-3 orders of magnitude below the CNS differential rate for silicon and germanium, respectively. With the acquisition of more simulated data, it is expected that the photon elastic scattering differential rate for both silicon and germanium will be higher than the dark matter scattering differential rate of Figure 1.1 for the whole γ-ray elastic scattering recoil energy ranges.

Chapter 5

Conclusion

γ-ray elastic scattering is an important background to consider for low-threshold dark matter direct detection. The simulation approximates a lower bound on the photon elastic scattering rate caused by ^{60}Co and ^{232}Th isotopes in the SuperCDMS SNOLAB housing. After implementing a recoil energy cutoff of 1 eV, this lower bound is ~ 0.01 and ~ 0.035 elastically scattered photons per year and kilogram for the silicon and germanium SuperCDMS detectors, respectively. This would be a significant background to proposed SuperCDMS detectors with ER/NR discrimination capabilities at eV-scale energies.

The *G4JAEAElasticScatteringModel* data files are not consistent with its documentation and the *SampleSecondaries* function does not take into account a factor of $2\pi \sin(\theta)$ when sampling the scattering angle. The *G4JAEAElasticScatteringModel* doesn't allow for energy deposits from its processes into the target material. As a result, the *CDMSJAEAElasticScatteringModel* was created in order to add the energy deposit functionality to the model. The problems with the JAEA data files and the *SampleSecondaries* function have not been fixed in the implementation of the *CDMSJAEAElasticScatteringModel*. Therefore, this should be considered when looking at the differential scattering rates in Section 4.

In the future, further effort should be made to properly implement *CDMSJAEAElasticScatteringModel* into SuperSim. Fixing the *SampleSecondaries* method to account for the change of variables and further analysis of the data files is required.

Références bibliographiques

[1] R. Agnese, Anderson *et al.* : Search for low-mass weakly interacting massive particles with supercdms. *Phys. Rev. Lett.*, 112:241302, Jun 2014.

[2] R. Agnese, Anderson *et al.* : New results from the search for low-mass weakly interacting massive particles with the cdms low ionization threshold experiment. *Phys. Rev. Lett.*, 116:071301, Feb 2016.

[3] R. Agnese et others. (SuperCDMS Collaboration) : Projected sensitivity of the supercdms snolab experiment. *American Physical Society*, 2017.

[4] A. Aguilar-Arevalo *et al.* : Measurement of radioactive contamination in the high-resistivity silicon ccds of the damic experiment. *Journal of Instrumentation*, 10(08):P08014, aug 2015.

[5] A. J. Anderson, J. M. Conrad, E. Figueroa-Feliciano, K. Scholberg et J. Spitz : Coherent neutrino scattering in dark matter detectors. *Physical Review D*, 84(1), jul 2011.

[6] E. Aprile *et al.* : Material screening and selection for xenon100. *Astroparticle Physics*, 35(2):43–49, 2011.

[7] C. Arpesella *et al.* : Measurements of extremely low radioactivity levels in borexino. *Astroparticle Physics*, 18(1):1–25, 2002.

[8] F.T. Avignone *et al.* : Theoretical and experimental investigation of cosmogenic radioisotope production in germanium. *Nuclear Physics B - Proceedings Supplements*, 28(1):280–285, 1992.

[9] John N. Bahcall, Aldo M. Serenelli et Sarbani Basu : New solar opacities, abundances, helioseismology, and neutrino fluxes. *The Astrophysical Journal*, 621(1):L85, jan 2005.

[10] John N. Bahcall et Roger K. Ulrich : Solar models, neutrino experiments, and helioseismology. *Rev. Mod. Phys.*, 60:297–372, Apr 1988.

[11] M.J. Berger *et al.* : Xcom: Photon cross sections database. `https://www.nist.gov/pml/xcom-photon-cross-sections-database`, 2010.

[12] J. Billard, E. Figueroa-Feliciano et L. Strigari : Implication of neutrino backgrounds on the reach of next generation dark matter direct detection experiments. *Phys. Rev. D*, 89:023524, Jan 2014.

[13] Julien Billard *et al.* : Direct detection of dark matter—appec committee report*. *Reports on Progress in Physics*, 85(5):056201, apr 2022.

[14] S. Cebrián, H. Gómez, G. Luzón, J. Morales, A. Tomás et J.A. Villar : Cosmogenic activation in germanium and copper for rare event searches. *Astroparticle Physics*, 33(5):316–329, 2010.

[15] B. K. Chatterjee et S. C. Roy : Tables of Elastic Scattering Cross Sections of Photons in the Energy Range 50–1500 keV for All Elements in the Range $13 \leq Z \leq 104$. *Journal of Physical and Chemical Reference Data*, 27(6):1011–1215, 11 1998.

[16] S.Y.F. Chu, L.P. Ekström et R.B. Firestone : The lund/lbnl nuclear data search. `http://nucleardata.nuclear.lu.se/toi/`.

[17] The EDELWEISS Collaboration, E. Armengaud *et al.* : Measurement of the cosmogenic activation of germanium detectors in edelweiss-iii, 2016.

[18] The SuperCDMS Collaboration : Background explorer. `https://bgexplorer.pnnl.gov/supercdms/`.

[19] Bernd Crasemann : *Atomic inner-shell physics*. Springer Science & Business Media, 2013.

[20] Minoru Koide Devendra Lai, E d w a r d D . Goldberg : Cosmic-ray-produced silicon-32 in nature. *SCIENCE*, 1960.

[21] F. Duncan, A.J. Noble et D. Sinclair : The construction and anticipated science of snolab. *Annual Review of Nuclear and Particle Science*, 60(1):163–180, 2010.

[22] J. Engel : Nuclear form factors for the scattering of weakly interacting massive particles. *Physics Letters B*, 264(1):114–119, 1991.

[23] H. Falkenberg, A. Hünger, P. Rullhusen, M. Schumacher, A.I. Milstein et K. Mork : Amplitudes for delbrück scattering. *Atomic Data and Nuclear Data Tables*, 50(1):1–27, 1992.

[24] D Z Freedman, D N Schramm et D L Tubbs : The weak neutral current and its effects in stellar collapse. *Annual Review of Nuclear Science*, 27(1):167–207, 1977.

[25] G. Fricke, C. Bernhardt, K. Heilig, L.A. Schaller, L. Schellenberg, E.B. Shera et C.W. Dejager : Nuclear ground state charge radii from electromagnetic interactions. *Atomic Data and Nuclear Data Tables*, 60(2):177–285, 1995.

[26] Particle Data Group, R L Workman *et al.* : Review of Particle Physics. *Progress of Theoretical and Experimental Physics*, 2022(8), 08 2022. 083C01.

[27] Karl Theodor Hecht : *Quantum mechanics*. Springer Science & Business Media, 2012.

[28] Shunsaku Horiuchi, John F. Beacom et Eli Dwek : Diffuse supernova neutrino background is detectable in super-kamiokande. *Physical Review D*, 79(8), apr 2009.

[29] J. H. Hubbell et S. M. Seltzer : X-ray mass attenuation coefficients. `https://www.nist.gov/pml/x-ray-mass-attenuation-coefficients`, 2004.

[30] Carlo Jacoboni et Lino Reggiani : The monte carlo method for the solution of charge transport in semiconductors with applications to covalent materials. *Rev. Mod. Phys.*, 55:645–705, Jul 1983.

[31] WR Johnson et Kwok-tsang Cheng : Elastic scattering of 0.1-1-mev photons. *Physical Review A*, 13(2):692, 1976.

[32] M. H. Kelsey, R. Agnese, Y. F. Alam, I. Ataee Langroudy, E. Azadbakht, D. Brandt, R. Bunker, B. Cabrera, Y. Y. Chang, H. Coombes, R. M. Cormier, M. D. Diamond, E. R. Edwards, E. Figueroa-Feliciano, J. Gao, P. M. Harrington, Z. Hong, M. Hui, N. A. Kurinsky, R. E. Lawrence, B. Loer, M. G. Masten, E. Michaud, E. Michielin, J. Miller, V. Novati, N. S. Oblath, J. L. Orrell, W. L. Perry, P. Redl, T. Reynolds, T. Saab, B. Sadoulet, K. Serniak, J. Singh, Z. Speaks, C. Stanford, J. R. Stevens, J. Strube, D. Toback, J. N. Ullom, B. A. VanDevender, M. R. Vissers, M. J. Wilson, J. S. Wilson, B. Zatschler et S. Zatschler : G4cmp: Condensed matter physics simulation using the geant4 toolkit, 2023.

[33] F. J. Kerr et D. Lynden-Bell : Review of galactic constants. *Monthly Notices of the Royal Astronomical Society*, 221(4):1023–1038, 08 1986.

[34] Lynn Kissel : Rtab: the rayleigh scattering database. *Radiation Physics and Chemistry*, 59(2):185–200, 2000.

[35] Noah Kurinsky : *THE LOW-MASS LIMIT: DARK MATTER DETECTORS WITH EV-SCALE ENERGY RESOLUTION*. Thèse de doctorat, STANFORD UNIVERSITY, 2018.

[36] M. Laubenstein et G. Heusser : Cosmogenic radionuclides in metals as indicator for sea level exposure history. *Applied Radiation and Isotopes*, 67(5):750–754, 2009. 5th International Conference on Radionuclide Metrology - Low-Level Radioactivity Measurement Techniques ICRM-LLRMT'08.

[37] J.D. Lewin et P.F. Smith : Review of mathematics, numerical factors, and corrections for dark matter experiments based on elastic nuclear recoil. *Astroparticle Physics*, 6(1):87–112, 1996.

[38] J.C. Loach, J. Cooley, G.A. Cox, Z. Li, K.D. Nguyen et A.W.P. Poon : A database for storing the results of material radiopurity measurements. *Nuclear Instruments and Methods in Physics Research Section A: Accelerators, Spectrometers, Detectors and Associated Equipment*, 839:6–11, 2016.

[39] D.-M. Mei et A. Hime : Muon-induced background study for underground laboratories. *Phys. Rev. D*, 73:053004, Mar 2006.

[40] G. J. Neary et John Douglas Cockcroft : The β-ray spectrum of radium e. *Proceedings of the Royal Society of London. Series A. Mathematical and Physical Sciences*, 175(960):71–87, 1940.

[41] Live chart of nuclides: nuclear structure and decay data. `https://www-nds.iaea.org/relnsd/vcharthtml/VChartHTML.html`.

[42] Mohamed Omer et Ryoichi Hajima : Including delbrück scattering in geant4. *Nuclear Instruments and Methods in Physics Research Section B: Beam Interactions with Materials and Atoms*, 405:43–49, 2017.

[43] Mohamed Omer et Ryoichi Hajima : Geant4 physics process for elastic scattering of γ-rays. Rapport technique, Japan Atomic Energy Agency, 2018.

[44] Christian Ouellet et Balraj Singh : Nuclear data sheets for a = 32. *Nuclear Data Sheets*, 112(9):2199–2355, 2011.

[45] Ruslan Podviianiuk : The supercdms experiment overview, May 2022.

[46] Stefano Profumo : *An Introduction to Particle Dark Matter*. World Scientific Publishing Europe Ltd., 2017.

[47] Alan E. Robinson : Coherent photon scattering background in sub-GeV/c^2 direct dark matter searches. *Phys. Rev. D*, 95:021301, Jan 2017.

[48] F. Rohrlich et R. L. Gluckstern : Forward scattering of light by a coulomb field. *Phys. Rev.*, 86:1–9, Apr 1952.

[49] Ralph Schönrich, James Binney et Walter Dehnen : Local kinematics and the local standard of rest. *Monthly Notices of the Royal Astronomical Society*, 403(4):1829–1833, apr 2010.

[50] D. Aristizabal Sierra, Jiajun Liao et D. Marfatia : Impact of form factor uncertainties on interpretations of coherent elastic neutrino-nucleus scattering data. *Journal of High Energy Physics*, 2019(6), jun 2019.

[51] M. C. Smith *et al.* : The RAVE survey: constraining the local galactic escape speed. *Monthly Notices of the Royal Astronomical Society*, 379(2):755–772, aug 2007.

[52] Louis E Strigari : Neutrino coherent scattering rates at direct dark matter detectors. *New Journal of Physics*, 11(10):105011, oct 2009.

[53] Nicolò Trevisani : Collider searches for dark matter (atlas + cms). *Universe*, 4(11), 2018.

[54] S. Yellin : Finding an upper limit in the presence of an unknown background. *Phys. Rev. D*, 66:032005, Aug 2002.